The Astrophysical Journal, 799:192 (21pp), 2015 February 1 doi:10.1088/0004-637X/799/2/192

SIMULTANEOUS MULTIWAVELENGTH OBSERVATIONS OF MAGNETIC ACTIVITY IN ULTRACOOL DWARFS. IV. THE ACTIVE, YOUNG BINARY NLTT 33370 AB (= 2MASS J13142039+1320011)

P. K. G. Williams[1], E. Berger[1], J. Irwin[1], Z. K. Berta-Thompson[2], and D. Charbonneau[1]
[1] Harvard-Smithsonian Center for Astrophysics, 60 Garden Street, Cambridge, MA 02138, USA; pwilliams@cfa.harvard.edu
[2] MIT Kavli Institute, 77 Massachusetts Avenue, Cambridge, MA 02139, USA
Received 2014 September 15; accepted 2014 November 24; published 2015 January 29

ABSTRACT

We present multi-epoch simultaneous radio, optical, Hα, UV, and X-ray observations of the active, young, low-mass binary NLTT 33370 AB (blended spectral type M7e). This system is remarkable for its extreme levels of magnetic activity: it is the most radio-luminous ultracool dwarf (UCD) known, and here we show that it is also one of the most X-ray luminous UCDs known. We detect the system in all bands and find a complex phenomenology of both flaring and periodic variability. Analysis of the optical light curve reveals the simultaneous presence of two periodicities, 3.7859 ± 0.0001 and 3.7130 ± 0.0002 hr. While these differ by only $\sim$2%, studies of differential rotation in the UCD regime suggest that it cannot be responsible for the two signals. The system's radio emission consists of at least three components: rapid 100% polarized flares, bright emission modulating periodically in phase with the optical emission, and an additional periodic component that appears only in the 2013 observational campaign. We interpret the last of these as a gyrosynchrotron feature associated with large-scale magnetic fields and a cool, equatorial plasma torus. However, the persistent rapid flares at all rotational phases imply that small-scale magnetic loops are also present and reconnect nearly continuously. We present a spectral energy distribution of the blended system spanning more than 9 orders of magnitude in wavelength. The significant magnetism present in NLTT 33370 AB will affect its fundamental parameters, with the components' radii and temperatures potentially altered by $\sim$+20% and ~-10%, respectively. Finally, we suggest spatially resolved observations that could clarify many aspects of this system's nature.

Key words: stars: activity – stars: individual (NLTT 33370) – stars: low-mass

1. INTRODUCTION

Low-mass stars are the most common stars in the universe (Reid & Gizis 1997), dominating the solar neighborhood in particular (Kirkpatrick et al. 2012). The ultracool dwarfs (UCDs) are those very low mass stars and brown dwarfs (BDs) with spectral types of M7 and later (Kirkpatrick et al. 1999; Martín et al. 1999), and they constitute comprise some of our closest neighbors (e.g., Luhman 2013, 2014). Despite this prevalence and proximity, there are significant gaps in our understanding of the nature of these objects, including their formation and multiplicity (Luhman 2012), internal structure (Baraffe et al. 2002), radiative output (Dupuy et al. 2009, 2014), atmospheric chemistry (Marley et al. 2013), magnetism (Williams et al. 2014; Cook et al. 2014), and rotational evolution (Irwin & Bouvier 2008; Reiners & Mohanty 2012; Gallet & Bouvier 2013).

Besides their intrinsic interest, these topics have received increased attention because low-mass stars are appealing host candidates for exoplanets (Scalo et al. 2007; Tarter et al. 2007), in particular Earth-like planets in the habitable zone (Bonfils et al. 2013; Kopparapu 2013). The inferred properties of such planets depend sensitively on those of their host stars, making accurate knowledge of the fundamental properties of the hosts a topic of paramount importance. Simultaneously, searches for the coolest UCDs are penetrating into regions of parameter space occupied by giant exoplanets amenable to direct imaging (e.g., Chauvin et al. 2005; Bowler et al. 2010; Patience et al. 2010; Barman et al. 2011; Delorme et al. 2012; Dupuy & Kraus 2013; Liu et al. 2013; Luhman 2014), driving interest in understanding the physical properties of these analogous populations.

The presence of magnetic activity in the UCD regime has important implications for both the fundamental physics of these objects and their role as exoplanet hosts and analogs. Magnetic fields alter their internal structures, affecting estimates of radii, temperatures, and mass by $\sim$5%–30% (Stassun et al. 2012), likely playing a role in explaining the frequent measurement of UCD radii that are significantly larger than those predicted by models (e.g., López-Morales 2007; Ribas et al. 2008; McLean et al. 2011; MacDonald & Mullan 2013). High flare rates and strong stellar winds will dramatically impact the location or existence of habitable zones around low-mass stars, prompting a significant amount of work investigating the magnetic (McIvor et al. 2006; Khodachenko et al. 2007; Lanza 2013; Llama et al. 2013; Cohen et al. 2011, 2014) and radiative (Segura et al. 2005; Lammer 2007; Lecavelier des Etangs 2007; Tian 2009; Poppenhaeger et al. 2013; Linsky et al. 2014; Shkolnik & Barman 2014) interactions between stars and planets.

The generation of magnetic fields in UCDs, however, is not clearly understood. UCDs are fully convective (Chabrier & Baraffe 2000) and thus lack a tachocline, the shearing interface between stellar radiative and convective zones that is understood to play a vital role in the generation of magnetic fields in Sun-like stars (Ossendrijver 2003). Early theoretical work supported the idea that these objects would therefore not be able to generate large-scale magnetic fields via dynamo action (Durney et al. 1993). The detection of radio bursts from the young BD LP 944-20, however, demonstrated that large-scale fields could in fact be present (Berger et al. 2001), and subsequent observations have established this using a wide range of techniques (Berger 2002, 2006; Burgasser & Putman 2005; Hallinan et al. 2006; Reiners & Basri 2006, 2007, 2010; Morin et al. 2010; Route & Wolszczan 2012). More recent simulations have also demonstrated the generation of large-scale magnetic fields in fully convective systems (Chabrier & Küker 2006; Dobler et al. 2006; Browning 2008; Brown et al. 2010a).

Observational tracers of UCD magnetism also present puzzles. The radio detection of LP 944-20, for instance, was a surprise, because it exceeded predictions based on the empirical Güdel–Benz relation (GBR; Güdel & Benz 1993; Benz & Güdel 1994) between the radio and X-ray luminosities of magnetically active stellar systems by more than four orders of magnitude (Berger et al. 2001). Subsequent observations have revealed that ∼5%–10% of UCDs are similar outliers, and the origin of this divergence remains unclear (Stelzer et al. 2012; Williams et al. 2014). Other observational tracers of magnetic activity, on the other hand, fade away dramatically in UCDs. Chromospheric activity as traced by Hα emission is generally "saturated" at luminosities of $L_{\rm H\alpha}/L_{\rm bol} \sim 10^{-3.5}$ in dMe flare stars, but this ratio decreases rapidly in the UCD regime (Gizis et al. 2000; West et al. 2004; Berger et al. 2010). X-ray emission follows a similar pattern, with typical luminosities decreasing from a saturation value of $L_{\rm X}/L_{\rm bol} \sim 10^{-3}$ (Vilhu 1984; Pizzolato et al. 2003) to virtually undetectable levels in L dwarfs (Stelzer et al. 2006a; Berger et al. 2008a, 2010; Williams et al. 2014); Kelu-1 AB is the only such object to be detected, with 3–4 photons from *Chandra* (Audard et al. 2007). In each of these bands, the relationship between rotation and magnetic activity evolves significantly from what is found for earlier-type dMe stars, showing no saturation in the radio, the appearance of weakly emitting rapid rotators in Hα, and an anti-correlated "super-saturation" relationship in X-rays (Mohanty & Basri 2003; Berger et al. 2008a, 2010; Reiners & Basri 2010; McLean et al. 2012; Cook et al. 2014). Possible physical underpinnings of these trends include the increasing neutralization of the outer layers of the (sub)stellar atmosphere (Mohanty et al. 2002) or a shift in the topology of the large-scale magnetic field (Donati et al. 2008; Morin et al. 2008b, 2010). An understanding of the dynamo in the lowest-mass stars and BDs should lead to insight into the magnetic properties of massive exoplanets themselves.

Simultaneous multi-wavelength observations of activity tracers yield insight into a wide range of topics such as the chromospheric heating mechanism (Berger et al. 2008b), the magnetic field topology (Berger et al. 2008a), and role of variability in biasing empirical relationships between activity tracers (Berger et al. 2010). Here we present a detailed study of the active, young binary NLTT 33370 AB (= 2MASS J13142039 + 1320011) using simultaneous observations in the radio, optical, Hα, UV, and X-ray bands. NLTT 33370 AB is a unique system in terms of both its fundamental physical parameters and its magnetic properties. It is a tight, low-mass binary ($a \sim 2$ AU, $M_{\rm tot} \sim 200$ $M_{\rm J}$; Schlieder et al. 2014) resolvable with adaptive optics, so that it promises to become one of a small sample of benchmark UCD systems with dynamically measured component masses (Bouy et al. 2008; Dupuy et al. 2010; Konopacky et al. 2010). Unlike most other such systems, NLTT 33370 AB is young, with an estimated age of ∼30–200 Myr (Schlieder et al. 2014). This youth may be related to another dramatic characteristic: it is phenomenally magnetically active. It the most radio-luminous UCD system known (McLean et al. 2011), and, as we demonstrate in this work, it is also one of the brightest in X-ray and Hα emission, with frequent flaring across the electromagnetic spectrum.

We proceed by reviewing the observed and inferred properties of NLTT 33370 AB (Section 2). We then describe the observations (Section 3) and their analysis (Section 4), which yield a rich multi-wavelength data set with complex phenomenology that we summarize in Section 5. We discuss the implications of the data for the system's physical configuration and emission processes in Section 6. Finally, we summarize our findings and present our conclusions in Section 7.

Throughout this work, we use the notation $[x] \equiv \log_{10} x$, with x being measured in cgs units unless specified otherwise. Bolometric luminosities ($L_{\rm bol}$) are measured in units of $L_\odot$. Parentheses following numbers indicate uncertainties in the final digits; for instance, 123.4(56) is shorthand for 123.4 ± 5.6. To avoid linguistic contortions we will sometimes refer to NLTT 33370 AB as a single object; depending on the context, such references should be taken to mean either the blended system or a single but unspecified component of the binary.

2. NLTT 33370 AB

NLTT 33370 AB was originally identified as a high-proper-motion object in the New Luyten Two-Tenths catalog (Luyten 1979). It was subsequently recovered by Lépine & Shara (2005), who gave it the identifier LSPM J1314 + 1320. Further followup assigned a blended spectral type of M7.0e, a tangential velocity of 23.8(11) km s^{-1}, and a distance of 16.39(75) pc via trigonometric parallax (Lépine et al. 2009). Lépine et al. (2009) also measured an Hα equivalent width[3] (EW(Hα)) of 54.1 Å. Lucky imaging of NLTT 33370 AB resolved it into a binary with a separation of 0.13(2) arcsec (∼2.1 AU; ∼2500 R_*) and a companion ∼1 mag fainter than the primary in the i' band (Law et al. 2006). Although continued monitoring has refined the binary orbit, showing evolution in position angle (P.A.) and separations of ∼0.07 arcsec, the system parameters are still uncertain (Schlieder et al. 2014). A recent detailed analysis of the available astrometry, blended spectroscopy, and resolved photometry by Schlieder et al. (2014) has yielded estimates of $T_{\rm eff}$ = 3200(500) and 3100(500) K for the two components, masses of 97^{+41}_{-48} and 91^{+41}_{-44} $M_{\rm J}$, a system bolometric luminosity $[L_{\rm bol}] = -2.36(9)$ ($10^{31.2}$ erg s^{-1}), and a young system age of 30–200 Myr. NLTT 33370 AB may be a member of the nearby, young AB Dor moving group (Schlieder et al. 2012), but such an assignment is still tentative (Schlieder et al. 2014).

McLean et al. (2011) detected NLTT 33370 AB in the radio as part of a large VLA survey of UCDs (McLean et al. 2012). The emission was bright ($S_\nu \approx 1$ mJy at 4.86 GHz) and broadband ($S_\nu \approx 0.8$ mJy at 22.5 GHz). Furthermore, NLTT 33370 AB was detected at a similar flux density in the Faint Images of the Radio Sky at Twenty Centimeters survey (FIRST; Becker et al. 1995), indicating that the emission was stable over a ∼10 yr timescale. The radio emission varied sinusoidally with a period of 3.89(5) hr and amplitudes of ∼30% (20%) at 4.86 (8.46) GHz. At 4.86 GHz the periodicity was also detected in circular polarization (CP), with the polarization helicity alternating between left- and right-handed in phase with the total intensity. McLean et al. (2011) also obtained broadband optical photometry of NLTT 33370 AB from the MEarth survey (Nutzman & Charbonneau 2008; Berta et al. 2012) using the Monitor pipeline (Irwin et al. 2007), finding periodic modulation with a period of 3.785(2) hr and an amplitude of ∼15 mmag (∼1.4%). The optical periodicity is thus marginally shorter than the radio periodicity, differing by 6(3) minutes. Finally, McLean et al. (2011) obtained optical spectroscopy and measured $v \sin i = 45(5)$ km s^{-1} and, on two observing sessions separated by ∼100 days, Hα EWs of 9.9 and 14.6 Å.

[3] Throughout this work, we report EW(Hα) as a positive number; some authors, including Schlieder et al. (2014), choose to use negative values for spectral lines in emission. This work involves no discussion of absorption lines so there is no ambiguity.

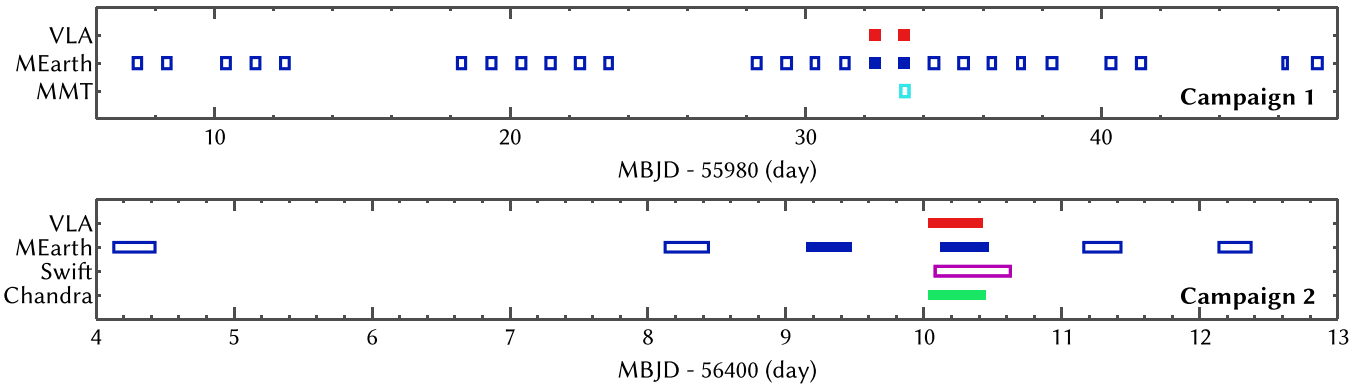

Figure 1. Overview of the observing campaigns. Filled blocks indicate observations with essentially continuous coverage, while outlined blocks indicate observations consisting of distinct snapshots. Note the differing horizontal scales; the individual MEarth observations have equal durations in both campaigns.

NLTT 33370 AB has also been observed in the radio using very long baseline interferometry (VLBI), a technique that can easily resolve the binary and could potentially resolve the radio emission from each binary component. McLean et al. (2011) report a detection of one unresolved source with a synthesized beam of size 2×1 mas, indicating that the emission originates from a region $\lesssim$50 R_* in size. Additional sources brighter than ∼0.2 mJy are excluded. Subsequent VLBI observations continue to reveal only a single radio source (J. Forbrich 2014, private communication). The system's astrometric parameters are not sufficiently well-known to identify whether the primary or the secondary is the radio source. Upcoming observations will measure these parameters more precisely (cf. Schlieder et al. 2014), resolving this question and allowing much more stringent constraints to be placed on the radio luminosity of the undetected source.

3. OBSERVATIONS AND DATA REDUCTION

We observed NLTT 33370 AB in two simultaneous multiwavelength campaigns in 2012 March and 2013 April. In Figure 1 we provide a graphical overview of the observations. The centerpiece of Campaign 1 (2012) was two consecutive 10 hr nights of intensive optical and radio observations, with additional optical spectroscopic observations on the second night. We performed additional optical monitoring observations over ∼20 days on either side of the intensive observations. The centerpiece of Campaign 2 (2013) was a 10 hr session of simultaneous broadband optical, radio, X-ray, and UV observations, again with additional broadband optical observations surrounding the period of intensive observing. Below, we describe the observations and data reduction in more detail.

The calibrated photometric data from the intensive observing sessions are shown in Figures 2 (Campaign 1) and 3 (Campaign 2). We have converted all timestamps to modified, barycentric Julian dates (MBJDs) in the barycentric dynamical time (TDB) timescale, which is the most appropriate system for long-term timing applications (Eastman et al. 2010). The integration times of the measurements presented in this work are all well above the ∼5 ms uncertainties in our conversion routines.

3.1. MEarth

We obtained long-term photometric monitoring of NLTT 33370 AB with telescopes in the MEarth array (Nutzman & Charbonneau 2008; Berta et al. 2012). The observations of Campaign 1 span from 2012 March 1 to April 10, covering 27 nights. Those of Campaign 2 span from 2013 April 22 to April 30, covering 6 nights. The observations were made with a long-pass RG715 Schott glass filter. This is the same configuration as used in the observations reported by McLean et al. (2011), but the instruments and filters were reconfigured in the interval between the two studies, so the bandpasses are likely slightly different. All observations were made with an exposure time of 42 s. The median FWHM in the Campaign 1 observations is 3.″1 (4.1 pixels); in Campaign 2, it is 2.″6 (3.4 pixels). This is somewhat smaller than in the observations of McLean et al. (2011) because MEarth operated with a slight defocus in the 2008–2009 observing season.

Most of the MEarth observations occurred with a cadence of ∼20 minutes over the course of each night. However, during two "intensive" nights in each campaign (indicated with filled boxes in Figure 1), observations were essentially continuous, with a cadence of 71 s. These nights were the ones in which the simultaneous monitoring at other bands occurred. The beginning of the first intensive night of Campaign 1 was affected by significant cloud cover, as is discernable in Figure 2. The other observations were generally performed in clear conditions.

We also used previous MEarth observations of NLTT 33370 AB, taken between 2010 February 13 and February 19 and described by McLean et al. (2011). These data were reprocessed with a newer version of the MEarth reduction pipeline than used in that work, but the changes in the outputs are minor. We refer to these measurements as originating in Campaign 0.

The raw MEarth images are processed automatically using the Monitor project pipeline (Irwin et al. 2007) with facility-specific improvements as described in the processing documentation for MEarth Data Release 2 (DR2).[4] The resulting tables of differential photometry are affected by three lingering systematic effects that can be described with the equation

$$m_{\rm true} = m_{\rm obs} + \sum_i k_{{\rm ZP},i}\,\delta(S-i) + k_{\rm CM}{\rm CM} + k_{\rm FWHM}({\rm FWHM} - {\rm FWHM}_0). \quad (1)$$

Here $m_{\rm true}$ is the true differential magnitude, $m_{\rm obs}$ is the observed value reported by the pipeline, the CM term refers to a "common mode" effect due to color-dependent extinction, and the FWHM term refers to seeing-dependent offsets in the photometry. The $k_{{\rm ZP},i}$ sum is a zero-point term: each MEarth instrument configuration or "segment" is assigned a unique integer identifier (denoted S above) and has its own zero point.

[4] http://www.cfa.harvard.edu/MEarth/DR2/processing/

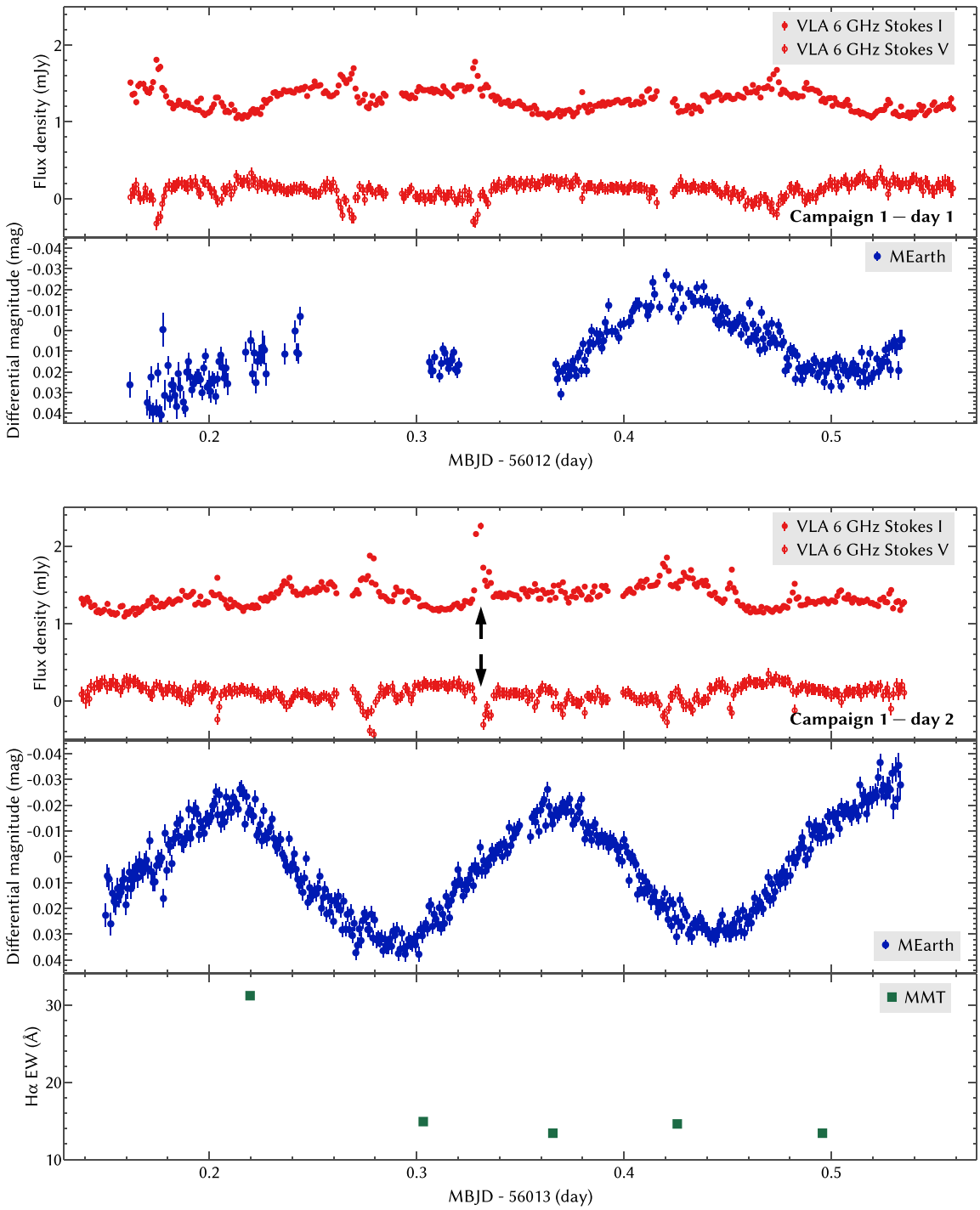

Figure 2. Calibrated radio, optical, and Hα data from Campaign 1. The upper pair of panels show the first day of intensive observations, while the lower triptych shows the second. The black arrows in the VLA day 2 panel indicate a fully polarized flare peaking at ~8 mJy that exceeds the plot bounds (see Section 4.2, Figure 8). The radio data have been smoothed to a cadence of 80 s for legibility. Section 4 presents a detailed analysis of these observations.

The MEarth DR2 release notes[5] contain much more detailed information on these effects.

The variables $m_{\rm obs}$, S, CM, and FWHM are output by the pipeline for each photometric measurement. In our data, $2 \leqslant S \leqslant 5$. The k variables are calibration terms that must be determined for each source by simultaneously modeling their values as well as the underlying source magnitudes $m_{\rm true}$. $\rm FWHM_0$ is an arbitrary constant that can aid the numerical stability of the modeling; it is degenerate with the $k_{{\rm ZP},i}$. The FWHM-dependent term is only significant for crowded fields, and we found in practice that the parameter $k_{\rm FWHM}$ was not well-constrained in our modeling. We therefore fixed it to zero, leaving five calibration parameters when modeling the three campaigns.

We discarded individual photometric measurements based on data quality metrics. Measurements in which the fitted source position was offset from its expected location by more than 12 pixels in either the x or y direction (table columns `Delta_X`,

[5] http://www.cfa.harvard.edu/MEarth/DR2/README.txt

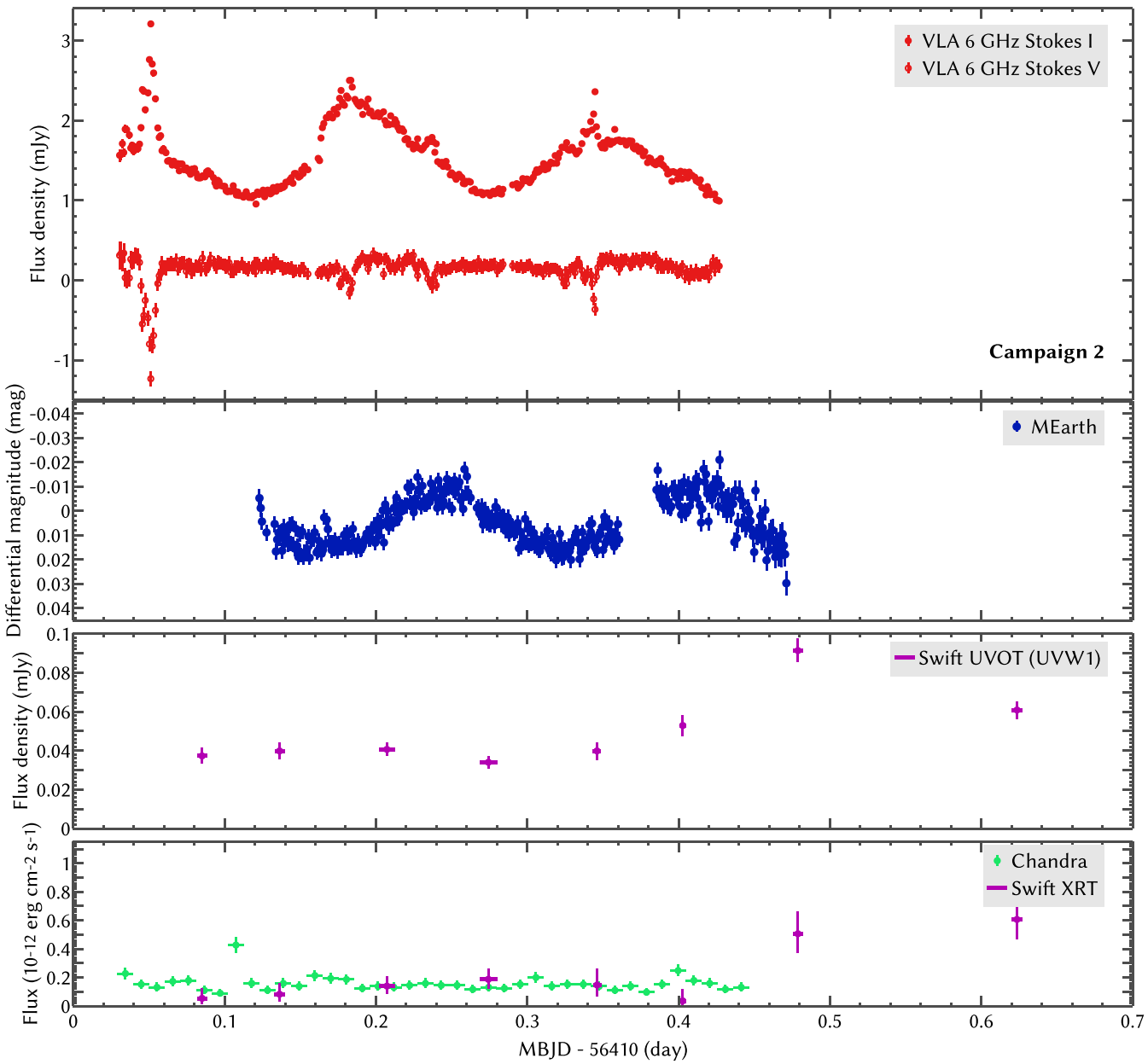

Figure 3. Calibrated radio, optical, UV, and X-ray data from the intensive segment of Campaign 2. The intensive MEarth observations from the previous day are not shown; they are similar to the ones here. X-ray fluxes are in the 0.2–2 keV band and represent counts binned at a 15-minute cadence. The radio data have been smoothed to a cadence of 80 s for legibility. Section 4 presents a detailed analysis of these observations.

`Delta_Y`) were rejected, as were those in which the estimated cloud extinction exceeded 1 mag (table column `DMag`). The locations of these cutoffs were determined empirically, and they eliminate 9% of the measurements. Cuts on other quantities (source ellipticity, FWHM, etc.) were investigated but were not found to be beneficial.

3.2. VLA

We monitored NLTT 33370 AB in the radio with the Karl G. Jansky Very Large Array (VLA) on the nights of 2012 March 26, 2012 March 27, and 2013 April 28 (projects VLA/12A-090 and SE0124; PI: Berger). The VLA was in the C configuration for first two nights (Campaign 1) and the D configuration for the third (Campaign 2). Each observing session lasted 10 hr and consisted of integrations on the target with periodic visits to a phase calibrator, J1309 + 1154, at a 9-minute cadence. In all cases, 3C286 was used as a bandpass, flux density, and polarization calibrator, with multiple visits over the course of the night allowing full polarimetric calibration. The integration time was 5 s and the *C* band receivers were used, with 2048 MHz of total bandwidth divided into two basebands centered at 5.0 and 7.1 GHz, each containing 512 spectral channels. In each night, the total integration time on the target was 496 minutes, or 83% of the session.

We additionally obtained multi-band radio photometry of NLTT 33370 AB with the VLA on the night of 2012 March 24 (project VLA/12A-090), just before the intensive monitoring observations of Campaign 1. The details of these observations and their outcome will be described in a forthcoming publication.

We calibrated the VLA data using standard procedures in the CASA software system (McMullin et al. 2007).

Radio-frequency interference was flagged automatically using the `aoflagger` tool, which provides post-correlation (Offringa et al. 2010) and morphological (Offringa et al. 2012) algorithms for identifying interference. Each observation included four visits to the calibrator 3C 286, allowing full polarimetric calibration. The flux density scale was referenced to 3C 286 using the preliminary, 2010 version of the scale defined by Perley & Butler (2013). After calibration, the data sets were time-averaged to a uniform cadence of 10 s.

To check data quality and develop a model of the radio emission from unrelated sources in the NLTT 33370 AB field, we imaged the data. For each night we made an image of 2048 × 2048 pixels, each $1''\times1''$. The imaging process used multi-frequency synthesis (Sault & Wieringa 1994) and CASA's multi-frequency CLEAN algorithm with 2250 iterations. Because of the wide bandwidth of the data, we used two spectral Taylor series terms for each CLEAN component, i.e., modeling both the flux and spectral index of each source. The reference frequency for these images is 6.05 GHz. We detected NLTT 33370 AB robustly at all times.

We then extracted photometry for NLTT 33370 AB from the visibility-domain data following the procedure described in Williams et al. (2013), using the deep images to establish a precise source position and model the radio emission in the field. The Stokes I and V light curves are plotted in Figures 2 and 3. Values of V greater (less) than zero denote right (left) circular polarization (RCP, LCP). We denote the fractional circular polarization $f_c \equiv V/I$. Stokes parameters are defined such that for any given emission component, $I \geqslant |V| \geqslant 0$ and $|f_c| < 1$. The Stokes parameters for the superposition of two components are simply sums: $I_{12} = I_1 + I_2$, $V_{12} = V_1 + V_2$. The radio data are all consistent with zero linear polarization.

Figure 4 shows the Stokes I photometry of NLTT 33370 AB for the two VLA basebands separately. The common vertical scale of the three panels makes clear the different variation patterns seen in Campaigns 1 and 2. The flat spectrum reported by McLean et al. (2011) is evident in the fact that in most cases the flux densities in the two basebands are virtually identical. The rapid flares, however, are generally brighter at lower frequencies. Conversely, the rising periods of the slow variation in Campaign 2 are associated with brighter emission in the 7.1 GHz baseband.

3.3. Chandra

The *Chandra* observations were performed on 2013 April 28 (proposal 14200124; *Chandra* observation ID 14530; PI: Berger) using the S3 backside-illuminated chip of the ACIS imager. The total exposure was 35.6 ks, ranging from MBJD 56410.019–56410.457. No grating was used, the data mode was `VFAINT`, and the exposure mode was "timed" (TE).

We analyzed the *Chandra* data in CIAO version 4.6.1 (Fruscione et al. 2006) using CalDB version 4.5.9. Following `VFAINT` reprocessing to eliminate a substantial fraction of background events, we estimated the residual background in the data by extracting events in an energy range of 0.3–7 keV in a large annulus around the astrometrically predicted position of NLTT 33370 AB. The mean whole-chip background rate is 0.39 s^{-1}, which is consistent with typical nonflaring behavior. We performed a Bayesian blocks analysis (Scargle 1998; Scargle et al. 2013) to search for background flares as manifested by significant changes in the background count rate, using the implementation described in Williams et al. (2014). No such changes were found.

Based on the astrometric parameters given by Schlieder et al. (2014), the predicted location of NLTT 33370 AB at the time of the *Chandra* observation is α = 13:14:20.17, δ = +13:19:58.4, with an uncertainty of $\sim1''$. The *Chandra* data contain an X-ray source of 909 counts (0.3–7 keV) within a $5''$ aperture at α = 13:14:20.14, δ = +13:19:58.5 (separation of $\sim0\farcs5$). This aperture is expected to contain ∼4.2 background counts. We identify this source with NLTT 33370 AB.

3.4. Swift

NLTT 33370 AB was observed by *Swift* on 2013 April 28 (target of opportunity ID 4717) with the X-ray Telescope (XRT), UV/Optical Telescope (UVOT), and γ-ray Burst Alert Telescope (BAT). No sources were detected with the BAT. The UVOT had the UVW1 filter (∼2280–2930 Å) in place and the XRT was in photon-counting (PC) mode. A total of 5.0 ks were spent on-source, divided among 8 visits of durations varying between 384 and 975 s. As can be seen in Figure 3, the total time spanned by the observations was ∼13 hr, with the final two visits occurring after the end of the simultaneous VLA, MEarth, and *Chandra* observations.

We analyzed the *Swift* XRT data using `HEAsoft` version 6.15.1 with `CalDB` version 20140120. We calibrated and cleaned the low-level data with the `xrtpipeline` task. We then extracted source events from a region coincident with NLTT 33370 AB having a radius of 20 pixels. Over the duration of the observation, 59 events were detected in the region, with an expectation of ∼7 of those coming from the background. The bottom panel of Figure 3 shows the resulting *Swift* XRT light curve. Here the event rates have been converted into fluxes using an energy conversion factor (ECF) of 2.14×10^{-11} erg cm^{-2} $count^{-1}$, which was derived using PIMMS for a 0.7 keV APEC plasma. This is the temperature obtained in a fit to the *Chandra* data (Section 4).

We analyzed the *Swift* UVOT data using the same software stack as for the XRT. We used the `uvotmaghist` task to derive the light curve data shown in Figure 3. The uncertainties shown are sums in quadrature of the pipeline-reported systematic and statistical uncertainties, which are dominated by the latter. The UVW1 filter of the UVOT is susceptible to a "red leak" of optical light with wavelengths $\lesssim$ 4500 Å (e.g., Brown et al. 2010b). While these wavelengths qualify as "red" compared to the UV band, they are still quite blue compared to the photosphere of NLTT 33370 AB. Based on the UVW1−B color of NLTT 33370 AB, the estimates of Brown et al. (2010b) suggest that the contribution of the photosphere is <0.2 mag, and a convolution of the UVW1 bandpass with the representative photospheric model described in Section 5.1 yields a contribution of $\sim2 \times 10^{-17}$ erg s^{-1} cm^{-2} $Å^{-1}$, ∼10% of the observed value in the UVW1 band.

3.5. MMT

We obtained optical spectroscopic observations of NLTT 33370 AB on 2013 March 27 UT with the Blue Channel spectrograph mounted on the MMT 6.5 m telescope. Six 300 s exposures were obtained at regular intervals between 05:05 and 11:42 UT, in conjunction with day 2 of Campaign 1. The observations were obtained with the 1200 line mm^{-1} grating leading to a wavelength coverage of 5435–6750 Å at a resolution of about 1.5 Å.

We processed and analyzed the data using standard routines in IRAF, and measured Hα EWs using the task `splot`.

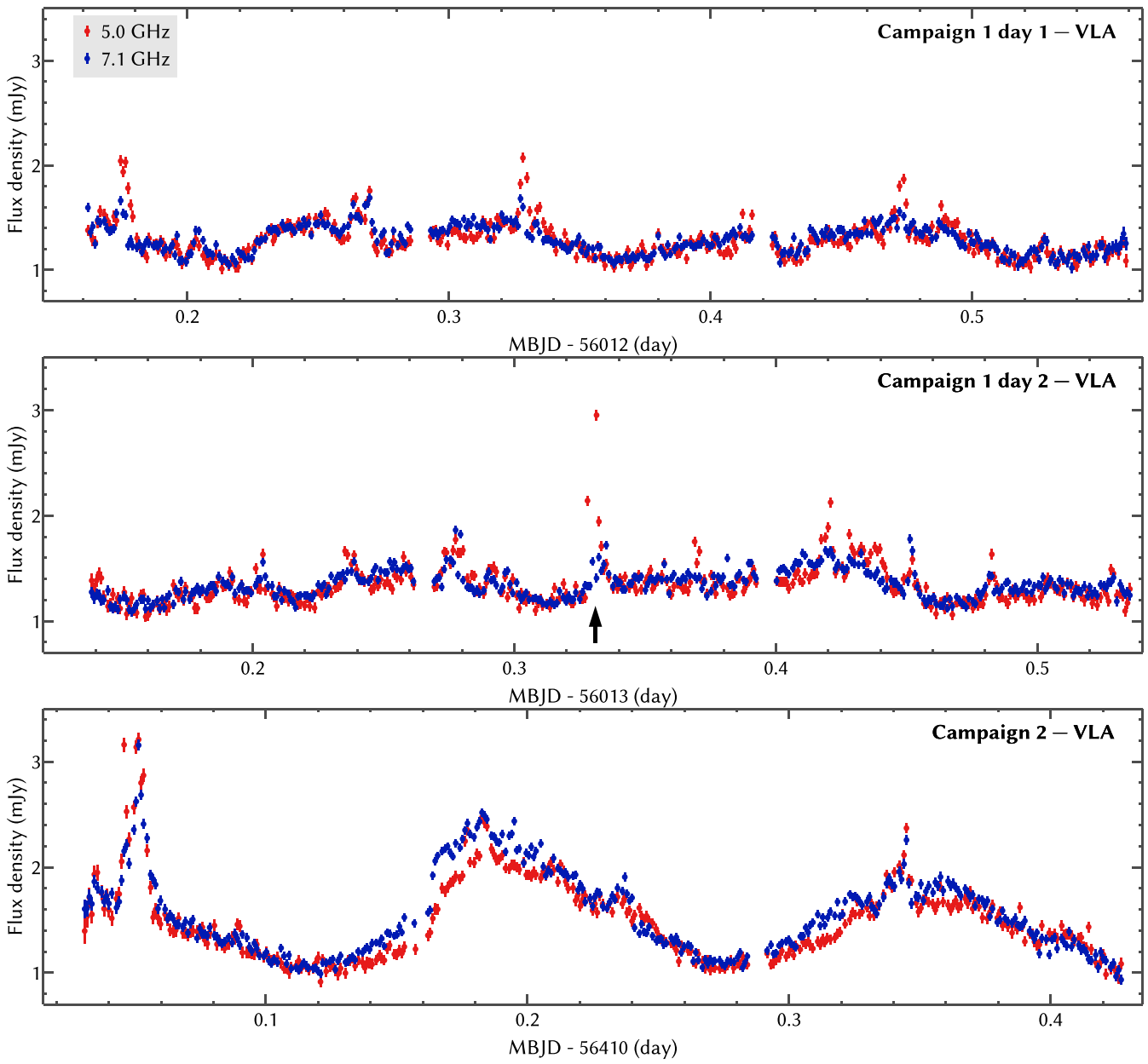

Figure 4. VLA Stokes *I* photometry separated by baseband: 5.0 GHz (red) and 7.1 GHz (blue). All panels are on equivalent horizontal and vertical scales, emphasizing the change in the radio behavior between the two campaigns. The black arrow indicates a fully polarized flare peaking at ∼8 mJy that exceeds the plot bounds (see Section 4.2, Figure 8).

The resulting values are plotted in Figure 2. The errors on each measurement are 0.15 Å.

4. ANALYSIS

We detected variable emission from NLTT 33370 AB in every observed band. We find both ubiquitous flaring and periodic, nonflaring modulations.

4.1. MEarth

The intensive MEarth observations in all three campaigns reveal sinusoidal variability. While the MEarth data do not show flares, examination of Figures 2 and 3 shows that there is variability on the ∼5 mmag level from one cycle to the next. Here we investigate the periodicities present in the MEarth data without attempting to model these low-level variations.

A single sine curve with a period of 3.779816(2) hr can reproduce the phasing of the observations very well over the full 3.4 yr time baseline of the data. A standard weighted nonlinear least-squares fit to the data yields a large reduced χ^2 (χ^2_r) of 6.89, however, with periodic structure in the residuals of the intensive observations. Comparison of Figures 2 and 3 suggests that, at a minimum, the oscillation amplitude evolves from one campaign to another. We performed this fit (and all others in this section) with a Python implementation of the Levenberg–Marquardt algorithm based on the classic `MINPACK` version (Moré 1978).

A sine curve model with a single period but different amplitudes and phases for each campaign achieves an improved $\chi^2_r = 4.28$ but still shows periodic residuals. Adding a second sine term yields $\chi^2_r = 2.65$ with much less marked structure in the residuals. The derived periods in this model are 3.7859(1)

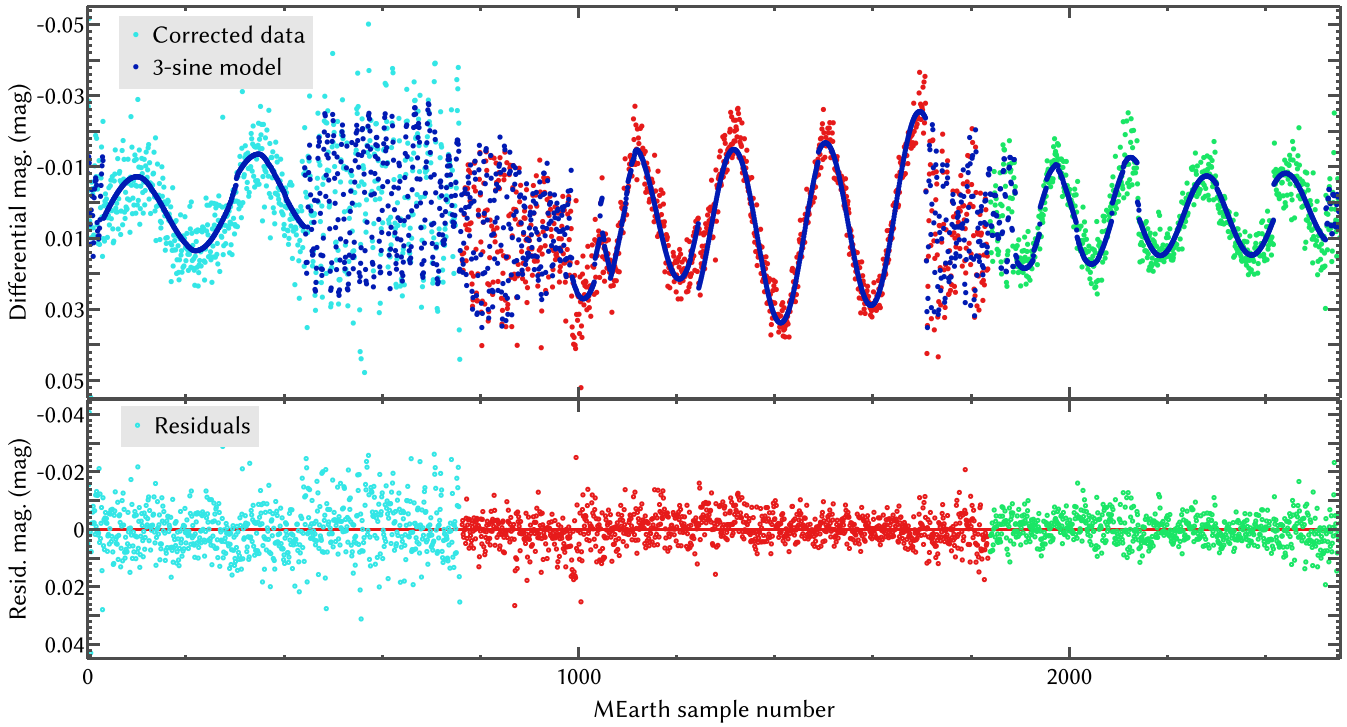

Figure 5. Data, model, and residuals for the complete MEarth data set. For clarity, the abscissa is a monotonically increasing sample number rather than, e.g., the observation time; the data span 3.4 yr. Data and residuals from Campaigns 0, 1, and 2 are shown in light blue, red, and green, respectively. The model is shown in dark blue. The "intensive" observing runs are apparent as segments of smoothly varying data. The data shown here have been corrected for MEarth photometric systematics as described in Sections 3.1 and 4.1.

and 3.7130(2) hr. The former value is consistent with the period of 3.785 hr derived by McLean et al. (2011) from the Campaign 0 data alone. A third sine term yields $\chi_r^2 = 2.24$ with the new period being 23.884(9) hr. This is close to the sidereal period (23.93 hr), suggesting that this component represents a systematic effect. The addition of a fourth term yields a marginal improvement ($\chi_r^2 = 2.21$). We use the 3-sine model to guide our interpretation of the data, treating the first two periodicities as astrophysical and the third as a systematic. The longer-period astrophysical term always has the higher amplitude and we refer to it as the "primary" component, while the shorter-period term is the "secondary." The 3-sine model and residuals are shown in Figure 5 and the derived parameters are listed in Table 1, where the sinusoidal components are given by

$$m_{\rm true} = A_i \sin\left(\frac{2\pi(t - T_i)}{P_i}\right). \quad (2)$$

Parameter uncertainties are derived from the covariance matrix determined by the Levenberg–Marquardt minimization. Because this model is defined in terms of magnitudes, maxima in luminosity correspond to minima in $m_{\rm true}$. All plots of MEarth data in this work use y axes such that brighter emission is closer to the top of the plot.

A more flexible model in which the periods of the sine curves may also vary between each campaign yields an indistinguishable $\chi_r^2 = 2.22$. In this model, the best-fit periods are all consistent with those obtained above. We conclude that there is no evidence for ∼year-timescale evolution in the periodicities present in the data, but cannot rule out changes at the $\lesssim$0.5% level.

The phase offsets between the Campaign 1 and 2 signals are 25(25) deg for the primary periodicity and 20(40) deg for the secondary. Between Campaign 0 and 1 they are 60(45) and −20(80) deg, respectively. A model with constant phasing between the three epochs achieves an inferior $\chi_r^2 = 3.85$, with large residuals outside of the regions of intensive observations, suggesting that the least-squares optimizer converged on a

Table 1
Fitted Parameters from MEarth Modeling

Group (1)	Param. (2)	Units (3)	Value (4)	Uncert. (5)
Calibration parameters	$k_{\rm ZP,2}$	mag	−0.0066	0.0013
	$k_{\rm ZP,3}$	mag	0.0020	0.0013
	$k_{\rm ZP,4}$	mag	0.0093	0.0004
	$k_{\rm ZP,5}$	mag	0.0033	0.0004
	$k_{\rm CM}$	...	−1.46	0.04
Primary periodicity	P	hr	3.7859	0.0001
	A_0	mag	0.0167	0.0004
	A_1	mag	0.0164	0.0002
	A_2	mag	0.0111	0.0003
	T_0	MBJD	55,247.6729	0.0006
	T_1	MBJD	56,010.8746	0.0003
	T_2	MBJD	56,409.8242	0.0008
Secondary periodicity	P	hr	3.7130	0.0002
	A_0	mag	0.0067	0.0004
	A_1	mag	0.0095	0.0002
	A_2	mag	0.0051	0.0003
	T_0	MBJD	55,247.6148	0.0015
	T_1	MBJD	56,010.9399	0.0004
	T_2	MBJD	56,409.9439	0.0017
Systematic term	P	hr	23.884	0.009
	A_0	mag	0.0061	0.0010
	A_1	mag	0.0097	0.0004
	A_2	mag	0.0040	0.0004
	T_0	MBJD	55,247.9231	0.0353
	T_1	MBJD	56,011.0259	0.0055
	T_2	MBJD	56,410.0172	0.0147

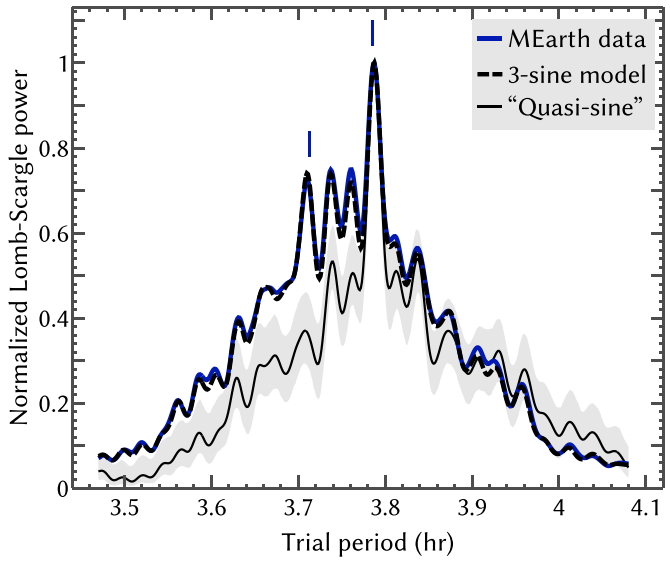

Figure 6. Lomb–Scargle periodograms for the Campaign 1 MEarth data. The periodogram for the systematics-corrected data is shown in blue with the peak normalized to unity. The dashed black line shows the normalized periodogram for the 3-sine model, using the same sampling as the data; it is nearly identical to the data periodogram. The thin black line shows the periodogram for a single-sine fit; its gray envelope shows the 90% credible region for a "quasi-sine" model with a single periodicity, but random amplitude and phase perturbations that vary with 2–400 hr autocorrelation timescales. See Section 4.1 for details. This model does not reproduce the observed periodogram structure. The short, vertical blue lines indicate the primary and secondary periods determined for the 3-sine model.

solution that worked unusually well for the densely sampled points, rather than a solution that fairly represented the overall system light curve.

We investigated whether the dual period results might be due to variations that are not strictly periodic (and hence are broadened in Fourier space) rather than two discrete components. In particular, we explored an alternative "quasi-sine" model in which A and T in Equation (2) wander randomly in time (i.e., possibly corresponding to a long-lived photospheric feature with evolving size and longitude). We realized 512 such models by drawing the amplitude and phase curves from squared-exponential Gaussian processes, in which the covariance C between measurements separated by an interval Δt is

$$C(\Delta t) = a \exp\left(\frac{\Delta t}{2s}\right)^2. \quad (3)$$

We drew a uniformly in log-space between 0.01 and 0.06 for the amplitude variation and between 0.01 and 0.1 rad for the phase variation. We drew s uniformly in log-space between 2 and 400 hr. The characteristic excursions were $\sim 10a$ in scale. We evaluated these models with the sampling of Campaign 1, which has the longest time baseline and most measurements of the three campaigns. Figure 6 compares Lomb–Scargle periodograms for the Campaign 1 data, the 3-sine model, and the quasi-sine realizations. The 3-sine model reproduces the observed periodogram well, while the quasi-sine realizations do not: they cannot recreate the asymmetry of the data periodogram.

The sum of two oscillations with frequencies f_1 and f_2 can be expressed as the product of two oscillations with frequencies $(f_1+f_2)/2$ and $(f_1-f_2)/2$. In this case the corresponding periods are 3.7491(1) hr and 16.07(4) days. Detailed investigation of the raw data does not reveal any evidence that the proximity of the long beat period to an integral number of days is due to a systematic. This periodicity is not prominent in the MEarth sampling pattern or any of the systematics parameters such as the CM "common mode" term. Efforts to model the data with a 16 day modulation term do not perform as well as the 3-sine fit (generally $\chi^2_r \sim 4.5$) and leave a persistent residual periodicity of $\sim$3.71 hr. We therefore conclude that the data require two periods separated by 4.37(1) minutes.

4.2. VLA

As previously found by McLean et al. (2011), the VLA photometry shows clear variability with a period comparable to that seen in the optical bands. At most times the emission has moderate RCP, with average values of $V = 0.14$ and 0.18 mJy outside of flares in Campaigns 1 and 2, respectively. Unlike the observations of McLean et al. (2011), however, rapid ($\sim$5 minutes), 100% left circular polarized (LCP) flares are observed superposed on the steadier emission in both Campaigns 1 and 2. Previous observations of the radio-active ultracool dwarf TVLM 513–46546 have revealed similar behavior: bright polarized bursts are sometimes observed (e.g., Hallinan et al. 2007) and sometimes excluded to high significance (e.g., Hallinan et al. 2006). One such flare, at MBJD $\sim$ 56,013.33, reaches a peak flux density of $\sim$8 mJy, which would have been clearly detectable in the data of McLean et al. (2011). We show this flare's dynamic spectrum in Figure 7 and a zoom-in of its light curve in Figure 8. The flare is completely absent from the upper baseband, with a cutoff frequency of $\sim$5.8 GHz suggested by extrapolation of the available data.

Such flares are generally interpreted as coherent radio emission (Hallinan et al. 2006, 2008; Berger et al. 2009; Route & Wolszczan 2012) arising from the electron cyclotron maser instability (ECMI; Wu & Lee 1979; Treumann 2006). In the ECMI paradigm, emission cuts off at approximately the cyclotron frequency $\nu_{\rm cyc} = eB/2\pi m_e c \approx 3(B/1{\rm kG})$ GHz. Given the results shown in Figure 7, this suggests $B \sim 2.1$ kG, in line with measurements of M dwarfs made through observations of Zeeman broadening of the magnetically sensitive FeH molecule (Reiners & Basri 2006, 2007, 2010). Taking a representative bandwidth of $\Delta\nu = 5.8$ GHz and flux density of 7 mJy, the flare luminosities reach $[L_{{\rm R},f}/L_{\rm bol}] \sim -6.1$, where $[L_{\rm bol}] = -2.36(9)$ Schlieder et al. (2014). Using a duration of 3 minutes (0.002 days), the flare energy output is $10^{27.4}$ erg.

To better understand the nonflaring emission, we subtracted the rapid LCP flares from the data as follows. First, we manually identified flare events by looking for abrupt simultaneous excursions in Stokes I and V. For each flare, we modeled the underlying nonflaring emission in both Stokes I and V with cubic polynomials $I_m(t)$ and $V_m(t)$ fitted to the surrounding flare-free measurements. For each in-flare measurement, we computed the flare intensity as the weighted mean of $I - I_m$ and $V_m - V$, then subtracted this quantity to obtain the nonflare residual. Although not required by our method, the modeled flare intensity is always consistent with being nonnegative. We investigated modeling of the flares with fractional circular polarizations that were high, but not 100%. The fits with 100% LCP were qualitatively the best, and are further justified by the near-perfect agreement between I and $-V$ seen in Figure 8. In Campaign 1, the 100% LCP flare duty cycle is 35(5)%, while it is 20(5)% in Campaign 2. The event rates are $\sim$0.9 hr^{-1} and $\sim$0.5 hr^{-1}, respectively.

The nonflaring component of the radio data shows quasi-periodic variations. We used phase dispersion minimization (PDM; Stellingwerf 1978) to identify a period of 3.787(1) hr

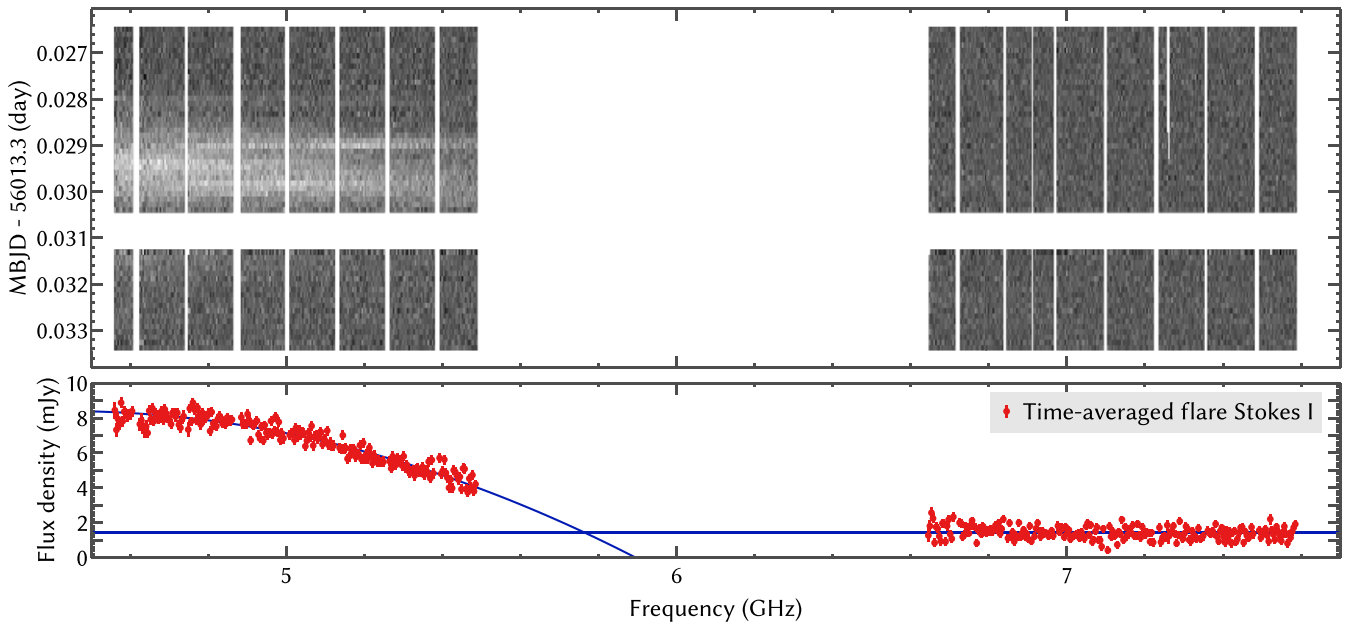

Figure 7. Upper panel: Stokes I dynamic spectrum of the bright radio flare seen in day 2 of Campaign 1. The measurements are made at a 10 s cadence and the grayscale runs linearly from −7.2 mJy (black) to 17.1 mJy (white). The large frequency gap in the data is due to the positioning of the VLA basebands; all others are due to RFI. The nonflaring variation has not been subtracted (Section 4.2). Lower panel: the flare spectrum averaged between $0.0286 < \mathrm{MBJD} - 56{,}013.3 < 0.0304$. The flare is absent from the 7.1 GHz frequency window. Also shown are parabolic (constant) fits to the spectrum in the lower (upper) frequency windows. These fits suggest that the flare cutoff frequency is ∼5.8 GHz. The flare light curve is shown in Figure 8.

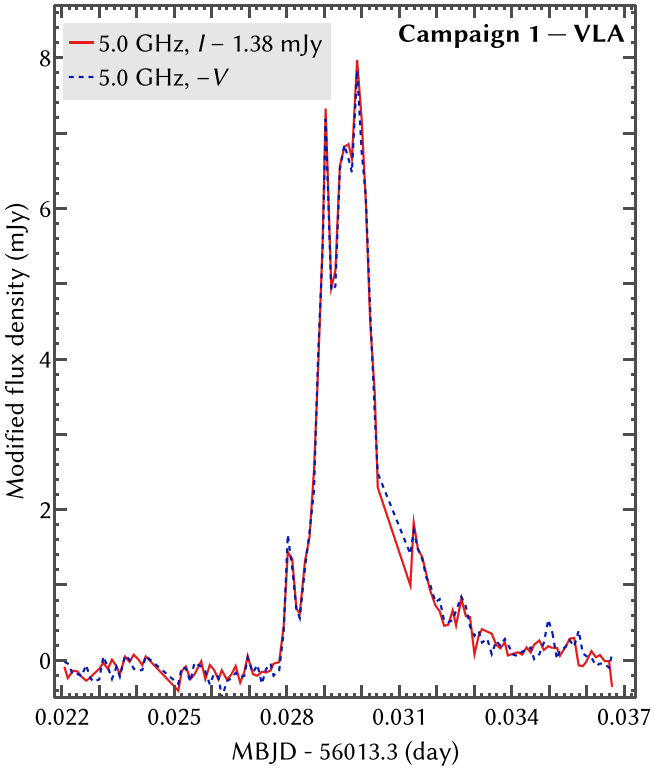

Figure 8. Light curve of the radio flare shown in Figure 7 averaging across the lower (5.0 GHz) baseband. Both Stokes I and V are shown. Because the flare is essentially 100% LCP, $-V$ is plotted to maintain positivity. The nonflaring, unpolarized emission has been removed by subtracting median$(I + V) = 1.38$ mJy from the Stokes I data. Errors are ∼0.1 mJy.

in the Campaign 1 Stokes I data, consistent with the primary MEarth periodicity, but different from the secondary periodicity at $\sim 70\sigma$. The PDM periodicity of the Campaign 2 Stokes V radio data is 3.75(5) hr; because the observation covered only ∼2.6 rotations, the precision is insufficient to make informative comparisons against the Campaign 1 or the MEarth results.

Figure 9 shows the VLA light curves after removal of the 100% LCP flares, along with indicators showing the phasing of the data with regard to the primary MEarth periodicity. We derived mean phase profiles for the Campaign 1 data by separately fitting smoothed cubic splines to the Stokes I, Stokes V, and f_c measurements after phasing them to this periodicity. Figure 9 shows both these mean profiles and the smoothed un-phased data. Disagreements between these curves indicate deviations from purely periodic variation. Disagreements are common even in the Campaign 1 Stokes I light curves: NLTT 33370 AB's radio emission modulates periodically but varies stochastically as well. We show the Campaign 1 mean phase profiles alongside the Campaign 2 data to aid comparison despite the time gap between the observations and the clear change in nature of the Campaign 2 Stokes I emission.

The non-flaring Stokes V radio emission in both campaigns is similar: it varies periodically in a sawtoothed pattern with a rapid rise and slow decay. In both campaigns the midpoint of the Stokes V decay phases with the maximum of the primary MEarth component, while the phasing with regards to the secondary MEarth component is not stable. There is a zero-point offset between the emission in the two campaigns, and the amplitude of the Campaign 2 variation is somewhat smaller: the smoothed flux density ranges between ∼−0.05–0.36 mJy in Campaign 1 and ∼0.02–0.33 mJy in Campaign 2. The Stokes V flux density and f_c do not differ significantly between the two VLA basebands at 5.0 and 7.1 GHz. The range of variation we observe is similar to that found at 8.5 GHz by McLean et al. (2011), although those authors were unable to detect a periodicity in that emission. At 4.9 GHz McLean et al. (2011) found periodic variation with $-0.3 \lesssim V \lesssim 0.2$ mJy, i.e., extending to significantly more net LCP than we observe. This difference may be due to the presence of low-level LCP flares in their data comparable to the ones we have removed,

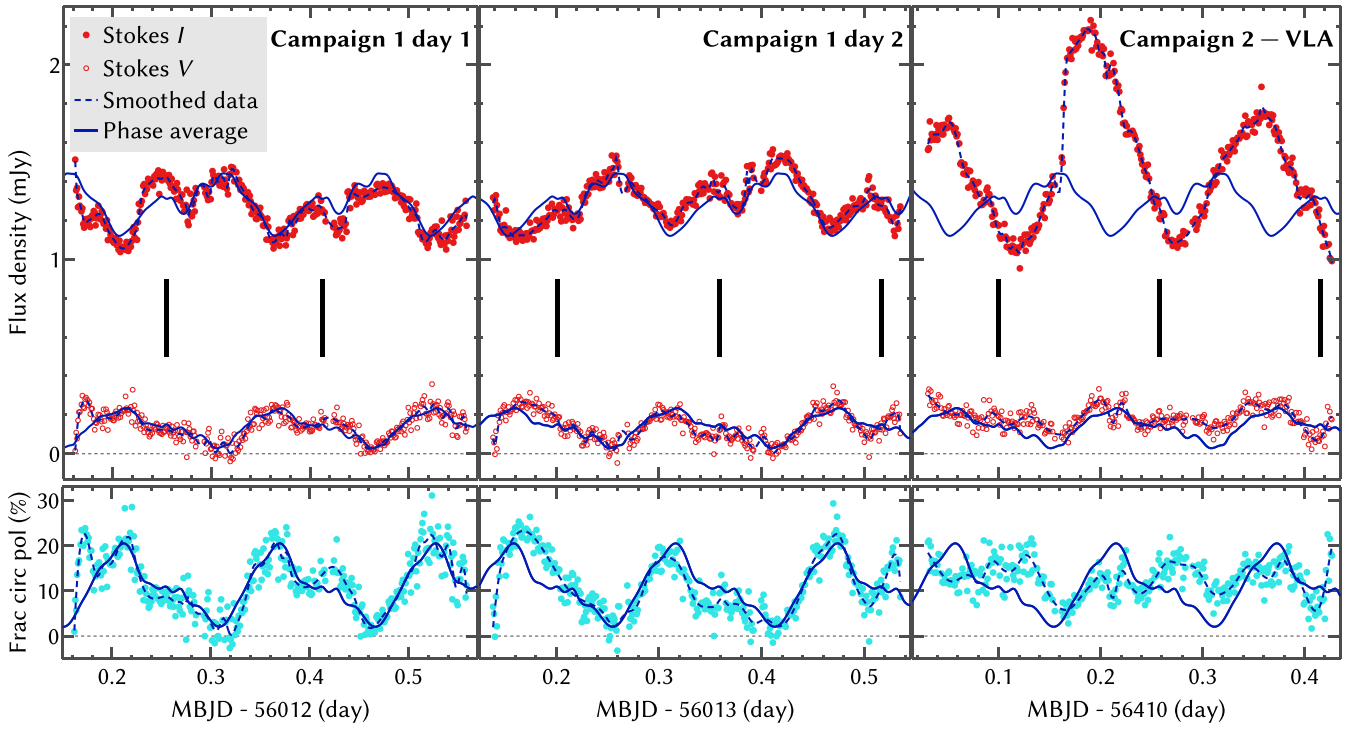

Figure 9. VLA light curves with 100% LCP flares removed. Stokes *I*, Stokes *V*, and f_c are shown. Vertical black lines indicate times of maximum flux in the primary MEarth periodic component. Dashed blue lines show smoothed spline fits to the data. Solid blue lines trace mean profiles of the Campaign 1 data after phasing to the primary MEarth periodicity (see Section 4.2). While the Campaign 2 Stokes *I* data disagree with the Campaign 1 mean phase profile, the Stokes *V* data show broadly similar structure.

but the sensitivity of the pre-upgrade VLA is insufficient to determine this; we note that these flares are more significant at lower frequencies (Figures 4, 7). In the non-flaring data $0 \lesssim f_c \lesssim 25\%$, also consistent with the 8.5 GHz results of McLean et al. (2011).

The nonflaring Stokes *I* radio emission of Campaign 2, on the other hand, differs substantially from that of Campaign 1. Although the minimal nonflaring Stokes *I* flux densities in both campaigns are ∼1.0 mJy, the maximum in Campaign 2 is ∼2.2 mJy, against ∼1.6 mJy in Campaign 1. While the Campaign 1 emission shows a sawtoothed, double-humped light-curve structure that mirrors the Stokes *V* variation, in Campaign 2 the variation is more uniform. As judged by the locations of the light curve minima, the phasing of the Stokes *I* emission relative to MEarth shifts by ∼180° between the two campaigns. McLean et al. (2011) measured flux densities somewhat lower than we do, finding $0.8 \lesssim I \lesssim 1.5$ mJy and $0.8 \lesssim I \lesssim 1.3$ mJy at 4.9 and 8.5 GHz, respectively. The emission maxima (minima) in that study are decreased (increased) compared to this work because of the longer averaging interval used (25 m versus ∼8 m). The modulation amplitudes are therefore also attenuated. The observed amplitudes are consistent with our Campaign 1 results but not those of Campaign 2.

Along with the phase shift relative to the optical emission, in Campaign 2 the rising portions of the nonflaring Stokes *I* light curve are associated with a rising spectrum, an effect not seen at any time in the Campaign 1 data (Figure 4). Meanwhile, as discussed, the Campaign 2 Stokes *V* light curve has a shape and phasing consistent with that of Campaign 1. These facts suggest the Campaign 2 radio emission may be the sum of a "Campaign 1" term and an additional component with $f_c = 0$. The phasing and evolution of this additional component imply that it arises from a distinct region and has a lifetime of at least a few rotations. As shown in Figure 9, however, the Campaign 2 Stokes *I* minima fall below what would be expected from Campaign 1. This could be due to the presence of an absorber, as discussed in Section 6.2.

The general phenomenology of the Campaign 2 Stokes *I* emission (temporary increase in flux density, rising spectrum) is suggestive of optically thick gyrosynchrotron flares. Assuming that the observed emission in these periods of Campaign 2 is the sum of a spectrally flat oscillating component and an unpolarized rising-spectrum flare component, we subtracted the former and applied standard gyrosynchrotron models and analysis (Dulk 1985; Osten et al. 2005) to the latter. Because this flare is assumed to be short-lived, its properties need not be consistent with those of the persistent emission (cf. McLean et al. 2011). We find $B \sim 500$ G, a brightness temperature $T_B \sim 10^9$ K, and a length scale of $\sim 1.7\ R_*$ for the emitting region. These results are in line with previous studies of similar objects (Berger 2002, 2006; Osten et al. 2002, 2005; Burgasser et al. 2013) and earlier work on NLTT 33370 AB (McLean et al. 2011). The length scale is compatible with spatially resolved VLBI observations of M dwarfs (Alef et al. 1997; Benz et al. 1998). We derive a number density of nonthermal ($E > 10$ keV) electrons $n_e \approx 6000$ cm^{-3}, with substantial uncertainties because the location of gyrosynchrotron spectral peak is weakly constrained. This value is consistent with the results of Osten et al. (2005) and several orders of magnitude smaller than typical estimates of overall (thermal and nonthermal) cool star coronal electron densities, generally found to be 10^8–10^{10} cm^{-3} (Ness et al. 2002, 2004).

The nonflaring Stokes *I* spectral luminosity in Campaign 1 ranges between $[L_{\nu,\mathrm{R}}] = 14.52(5)$ and $14.70(5)$, where the uncertainties are due to the source distance and thus are correlated between the two measurements. In Campaign 2 $[L_{\nu,\mathrm{R}}]$

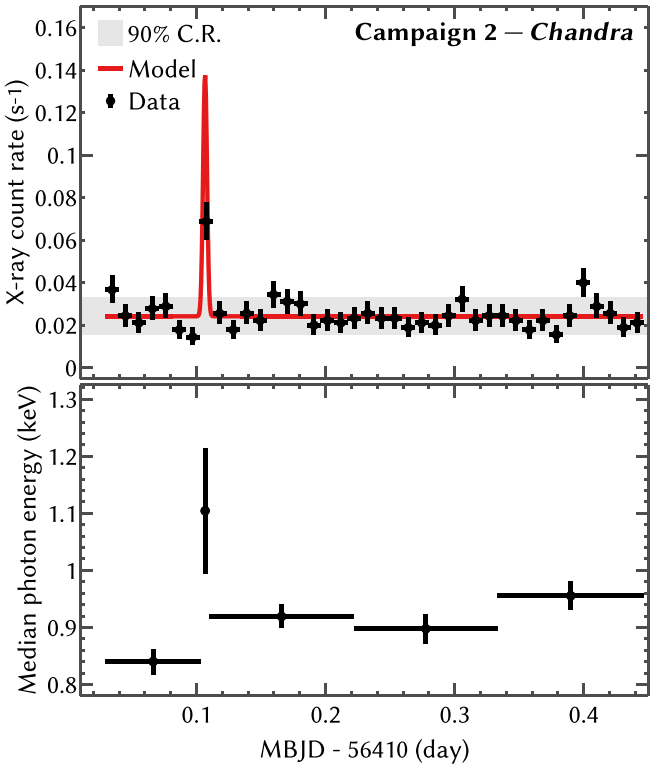

Figure 10. *Chandra* observations in Campaign 2. Black points in the upper panel show the count rate in uniform 15-minute bins. The red line shows an analytic model fit to the unbinned data (see Section 4.3). The gray band shows the 90% confidence region for samples of the quasi-quiescent emission; most of the apparent variability is not significant. The lower panel shows the change in the X-ray spectrum as quantified in the median photon energy (Hong et al. 2004). The increase in the hardness of the quasi-quiescent emission may be a precursor to the long-duration flare detected by *Swift*.

ranges between 14.48(5) and 14.86(5). Taking $[L_{\nu,\mathrm{R}}] \sim 14.6$ as a representative value we find $[L_{\nu,\mathrm{R}}/L_{\mathrm{bol}}] \sim -16.6$.

To summarize, the complex radio light curve of NLTT 33370 AB appears to combine emission from at least three separate components: rapid 100% LCP flares, periodically modulated emission with moderate RCP, and an additional unpolarized component seen only in Campaign 2. The complex morphology of the moderate RCP component implies that it further represents the combined emission of multiple regions or components. For instance, if the fact that the total intensity never drops below ∼1.0 mJy is taken as evidence for the presence of a constant component of that intensity, the periodic modulation in Campaign 1 would represent the emission of a component with $I \lesssim 0.4$ mJy. Furthermore, the mathematics of Stokes parameters (Section 3.2: $I \geqslant |V| \geqslant 0$ within each component) and anti-correlated variability in I and V then imply that the constant term has $f_c \sim 15\%$ while the modulating term has $f_c \sim -100\%$.

4.3. Chandra

Grouping the X-ray events into forty 15 minute bins suggests a largely steady source with at least one rapid flare (Figures 3 and 10). Figure 10 shows a 90% confidence region for the binned count rates assuming a steady source and Poisson statistics. The measurement at MBJD ∼ 56,410.11 is a 7.1σ outlier. The second-most outlying bin, at MBJD ∼ 56,410.40, contains 36 events and is a 2.9σ outlier. In 39 measurements there is a 7% chance of obtaining at least one value that large.

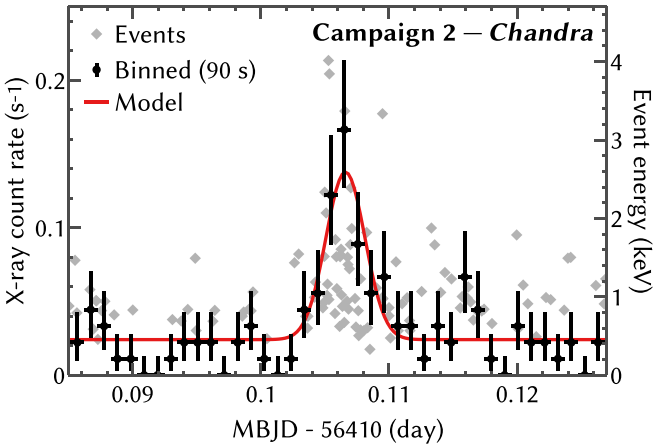

Figure 11. Zoom-in of the rapid X-ray flare. Along with the model as in Figure 10, individual events are shown with vertical positions indicating energy as shown on the right axis. Binned and model count rates are associated with the left axis. The binning interval is 90 s.

The red curve in the top panel of Figure 10 models the emission of NLTT 33370 AB as a constant ("quasi-quiescent") term plus a Gaussian flare. We determined the parameters for this model using a maximum-likelihood technique considering the arrival time of each observed photon. In particular, using a similar approach as the Bayesian Blocks technique, we performed a one-dimensional Voronoi tesselation of the photon arrival times and chose parameters to maximize the likelihood function of detecting one photon in each bin, evaluating the instantaneous rate function at each photon's observed arrival time. The fitted peak flux of the flare (above the quasi-quiescent level) is 0.11 counts s^{-1}. This is significantly above the corresponding 15-minute bin (Figure 10) because the modeled flare timescale is $\sigma = 2.2$ minutes. Figure 11 zooms in on the flare, showing a finer (90 s) binning as well as the arrival times and energies of the individual X-ray events.

The lower panel of Figure 10 shows the median photon energy in five time bins. This quantity provides a more robust quantification of the spectral shape than a traditional hardness ratio (Hong et al. 2004). The second bin encompasses the $\pm 2\sigma$ region of the flare, while the final three bins are uniform in size. Uncertainties on the medians are calculated using the method of Maritz & Jarrett (1978). The higher median photon energy in the flare bin is consistent with the general finding of elevated temperatures during such events (e.g., Robrade & Schmitt 2005). Strikingly, the median energy of the quasi-quiescent emission increases over the course of the observation. This may be a precursor to the slowly evolving flare captured by *Swift* after the end of the *Chandra* observations (Figure 3).

We modeled the overall X-ray spectrum of NLTT 33370 AB with `Sherpa` version 1 (Freeman et al. 2001). We used the `Sherpa` implementation of the Nelder & Mead (1965) simplex algorithm to optimize the C statistic of Cash (1979). We did not group the data in energy or subtract the (negligible) background. Photons with energies outside of the range 0.3–2.5 keV were ignored. We used the solar abundances of Lodders (2003). A two-temperature solar-abundance APEC (Astrophysical Plasma Emission Code; Smith et al. 2001) model yields a satisfactory fit, achieving a reduced statistic $C_r = 1.27$ with 146 degrees of freedom. We show the data and best-fit model in Figure 12. The temperatures of the two components are $kT = 0.27(2)$ keV and 1.20(6) keV, consistent with results seen in other active

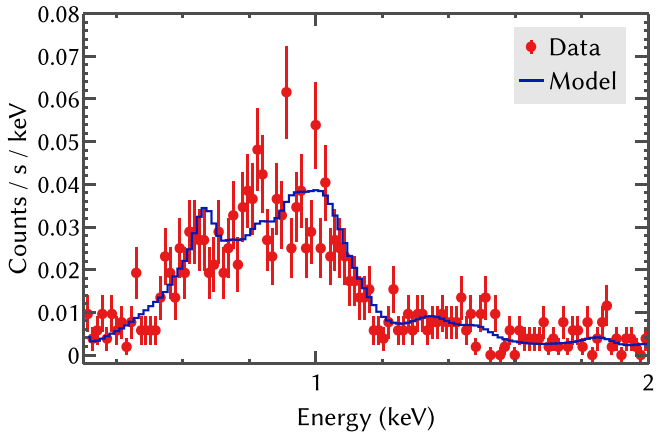

Figure 12. *Chandra* X-ray spectrum and a fitted two-temperature solar abundance APEC model. The temperatures of the two components are kT = 0.27(2) keV and 1.20(6) keV.

mid- to late M dwarfs (e.g., Robrade & Schmitt 2005; Williams et al. 2014). We note that, although there is evidence that the rapid flare has a hotter spectrum than the quasi-quiescent emission, it comprises ∼5% of the total number of observed events, and thus does not significantly affect the modeling. We have verified this by modeling only the events from the quasi-quiescent time periods. Table 2 reports the mean and peak X-ray fluxes based on our spectral modeling. The peak flux is derived assuming the same energy conversion factor (ECF; ratio of energy flux to count rate) as the mean emission, and thus may be slightly underestimated if the flaring spectrum is indeed hotter than the mean emission.

We investigated alternative models for the X-ray spectrum. In particular, high-S/N observations of active M dwarfs often reveal nonsolar elemental abundances, usually in the form of an inverse first ionization potential (IFIP) effect, in which elements with higher FIPs have elevated abundances (e.g., Robrade & Schmitt 2005). No single-temperature model with adjustable elemental abundances yields a superior fit to the data compared to the two-temperature solar-abundance model. Two-temperature models with adjustable elemental abundances show hints of an IFIP effect in NLTT 33370 AB, but the results are not statistically significant.

We also searched for periodicity in the nonflaring X-ray emission. As may be judged from Figure 10, any periodicity in the data must be weak, and requires statistical analysis to uncover. Unfortunately, the small number of observed rotations (∼2.6) means that statistical approaches have low sensitivity in this data set. Calculations of the Rayleigh test statistic (Kruger et al. 2002) showed that it simply correlated with the candidate rotation period in the parameter region of interest. The same outcome was found with the Kuiper V statistic (Kuiper 1960), a variant of the Kolmogorov–Smirnov test more suited for data on a circle. The available data do not provide significant evidence for periodicity in the X-ray emission.

We find $[L_{X,q}] = 27.71(5)$ and $[L_{X,f}] = 28.44(5)$, where the q and f subscripts denote quiescent and flaring states. (Here we consider the rapid X-ray flare observed by *Chandra*, and not the more poorly characterized event in the *Swift* data; both appear to have similar luminosities.) Unlike what is presented in Table 2, the flaring luminosity used here includes the contribution from the quiescent emission, for consistency with other studies. We find $[L_{X,q}/L_{bol}] = -3.5(1)$ and $[L_{X,f}/L_{bol}] = -2.8(1)$, comparable to the saturated X-ray emission seen in early-M dwarfs.

Table 2
Results of *Chandra* Analysis

State	Integ. Time (s)	Counts	$\langle f_X \rangle$ (erg s^{-1} cm^{-2})
(1)	(2)	(3)	(4)
Mean emission	35588	909	-12.80 ± 0.03
Flare peak	529	49	-12.15 ± 0.03

Notes. Column 4 is the X-ray flux in the 0.2–2 keV band. "Flare peak" measures the modeled peak excess above the quasi-quiescent emission.

The total energy output of the flare is $\sim 10^{30.9}$ erg. No counterpart is apparent in the radio data, while the MEarth and *Swift* data do not overlap this event. There is a suggestion of a rapid decrease in optical luminosity just after the flare in the MEarth photometry, but these points were observed in partially cloudy conditions and are not reliable enough to be conclusive. A similar rapid X-ray flare, with a timescale $\tau \lesssim 8$ minutes, was observed in the dM4.5e dwarf EV Lac (Osten et al. 2005), and some X-ray flares initially evolve on a similarly rapid timescale before shifting to slower decay (e.g., as seen on LP 412-31; Stelzer et al. 2006b). Assuming $kT = 1.2$ keV and thermal bremsstrahlung emission, the emission measure ($\mathrm{EM} = \int dV n_e^2$) corresponding to the peak luminosity is $\sim 6 \times 10^{51}$ cm^{-3}, in line with previous observations of flare stars (e.g., Schmitt & Liefke 2002; Robrade & Schmitt 2005; Stelzer et al. 2006b).

4.4. *Swift* XRT

The simultaneous *Swift* and *Chandra* data generally agree, with the exception of the *Swift* flux measurement at MBJD ∼ 56,410.4, which is substantially below that of *Chandra*. In particular, only one source event is detected in 380 s of observing. Its energy is 1.03 keV. During the precise *Swift* good-time interval ($0.4005 < \mathrm{MBJD} - 56{,}410 < 0.4049$), the *Chandra* count rate is consistent with the wider bin shown in Figure 10, as are the photon energies. We suspect an unidentified instrumental phenomenon during this *Swift* observation.

The two *Swift* observations occurring past the end of the VLA and *Chandra* monitoring suggest a substantial, slowly evolving (timescale ∼3 hr) flare. The median photon energies in these bins are 1.0(2) and 1.3(3) keV, suggesting a continuation of the hardening trend seen in the bottom panel of Figure 10. The observed X-ray luminosity in this event is compatible with that observed in the rapid *Chandra* X-ray flare, but the overall energy output would be larger by ≈2 orders of magnitude if the apparent timescale is accurate.

4.5. *Swift* UVOT

Similar to the XRT data, the UVOT measurements past the end of the simultaneous *Chandra*/VLA monitoring suggest a slowly evolving flare. Assuming a UVW1 filter bandwidth of 795 Å and pivot wavelength of 2517 Å (Breeveld et al. 2011), the flare luminosity peaks at $[L_{UVW1}] \sim 28.0$. It is tempting to infer a slow rise in UV luminosity in the period $56{,}410.3 \lesssim \mathrm{MBJD} \lesssim 56{,}410.5$, but we caution that the sparse sampling may mask more complicated variation. There is a ∼30% decline in the UV flux between the first and second samples of the flare light curve (MBJD ∼ 56,410.48 and 56,410.62, respectively). At this time, the X-ray light curve appears flat, although the measurement

uncertainty is nonnegligible. X-ray and UV variability often track each other fairly closely, with inter-band delays small compared to the timescales probed here (Osten et al. 2002, 2004; Mitra-Kraev et al. 2005; Berger et al. 2008a). The luminosity ratio between the two bands in this event is consistent with scaling relations found in simultaneous observations of flare stars (Mitra-Kraev et al. 2005).

The mean nonflaring luminosity is $[L_{\rm UVW1}] = 27.67(4)$, or $[L_{\rm UVW1}/L_{\rm bol}] = -3.6(1)$. Assuming a radius of 1.6(1) R_J (Schlieder et al. 2014), the surface flux is $[F_{\rm UVW1}] = 3.55(7)$ (erg s^{-1} cm^{-2} Å^{-1}), lying between typical values obtained for main-sequence and classical T Tauri stars (Johns-Krull et al. 2000) in a study performed at somewhat shorter wavelengths (1958 Å) and higher $T_{\rm eff}$ (3500–4500 K). While the nonflaring UVOT data are consistent with a constant flux ($\chi^2_r = 0.74$), their variations are suggestive of an oscillation with a periodicity similar to that of the MEarth data. Assuming a periodicity fixed to that of the primary MEarth component (3.7859 hr), we fit a sine curve to the UVOT data. The oscillation amplitude is 8(7)%, the phase relative to the primary MEarth component is 180(80) deg, and $\chi^2_r = 0.43$ (2 degrees of freedom).

4.6. MMT

The sparse time sampling of the MMT observations preclude a detailed analysis of the time variability of EW(Hα). We interpret the first measurement as a flare and the subsequent four as quiescent activity. In quiescence, EW(Hα) = 14.1(7) Å, an unusually high value compared to typical mid-to-late M dwarfs (e.g., Lee et al. 2010). This is consistent with the average value of EW(Hα) = 14.6 Å reported by McLean et al. (2011). Lépine et al. (2009) and Schlieder et al. (2014) find EW(Hα) = 54.1 and ∼50 Å, respectively, in single observations, suggesting frequent flares of luminosities a factor of ∼2 above what is contained in our observations.

We derive $L_{\rm H\alpha}$ from EW(Hα) using a "χ factor" approach, using the relation (Walkowicz et al. 2004)

$$\frac{L_{\rm H\alpha}}{L_{\rm bol}} = \chi \frac{\rm EW(H\alpha)}{1\ \text{Å}}. \quad (4)$$

Reiners & Basri (2008) determine $[\chi]$ as a polynomial function of $T_{\rm eff}$ in the mid-to-late M dwarf regime. Taking $T_{\rm eff}$ = 3150(500) K, we find $[\chi] = -4.4^{+0.2}_{-0.7}$. This is compatible with the value found using the polynomial fit to χ as a function of $V-I$ color given by West & Hawley (2008). It does not agree well with the value of χ reported by the latter authors for objects of spectral type M7 ($\chi \approx -5.3$); however, there is large scatter to their relation precisely at this spectral type, and it coincides with an inflection in their χ-vs-SpT data. We therefore prefer the Reiners & Basri (2008) computation. We find in quiescence that $[L_{\rm H\alpha}/L_{\rm bol}] = -3.3^{+0.2}_{-0.7}$ and that $[L_{\rm H\alpha}] = 27.9^{+0.2}_{-0.7}$. As may be expected from the large quiescent EW(Hα), the derived value of $[L_{\rm H\alpha}/L_{\rm bol}]$ is also unusually large compared to most M7 dwarfs, which typically have $[L_{\rm H\alpha}/L_{\rm bol}] = -4.7$ (West et al. 2004, 2011). McLean et al. (2011) find a lower but compatible value of $[L_{\rm H\alpha}/L_{\rm bol}] = -3.8$ for the quiescent emission from equivalent values of EW(Hα), indicating different values for χ and/or $L_{\rm bol}$.

Previous studies suggest that the Hα flare timescale is likely ∼10–100 minutes (Hilton et al. 2010; Lee et al. 2010). The observed magnitude of the flare can be assessed as max(EW(Hα))/ min(EW(Hα)) ≈ 2.3, consistent with observations of flare stars (Lee et al. 2010). There is no clear correlation with any variations in the radio band. While a 100% LCP flare occurs ∼20 minutes before the high Hα measurement, the radio events are sufficiently frequent that there is plausibly happenstance. It is somewhat surprising that the Hα event appears to take place around the maximum of the optical light curve: in a model in which the optical light curve is modulated by dark spots, presumed to be associated with enhanced magnetic activity, Hα would be expected to be correlated with optical minima, a trend that has been observed (Frasca et al. 2000).

The nonflaring Hα data suggest an oscillation with a periodicity similar to that of the MEarth data. Here, a fit at the secondary MEarth periodicity gives a better $\chi^2_r = 4.74$ (1 degree of freedom) compared to that at the primary periodicity, $\chi^2_r = 6.27$. We find an amplitude of 5.9(7)% and a phase relative to the secondary MEarth component of 120(20) deg. The relatively large values of χ^2_r and small parameter errors are driven by the small (0.15 Å) statistical error bars on the measurements of EW(Hα).

5. SUMMARY OF THE PHENOMENOLOGY

5.1. Spectral Energy Distribution

Table 3 summarizes several key parameters regarding the emission of NLTT 33370 AB in the radio, broadband optical, Hα, UV, and X-ray bands. The optical luminosity is computed for the R band assuming the k-corrections of Blanton & Roweis (2007). The nonflaring radio parameters are derived for the Stokes I emission and the flare parameters refer to the rapid 100% LCP events. The UV and X-ray flare parameters refer to the slowly evolving event detected by *Swift*. The parameters for the flares outside of the radio band are uncertain because only portions of single events were observed.

NLTT 33370 AB is the brightest UCD in terms of radio flux density (with the nearest rival being LSPM J1835+3259 at 525(15) μJy in quiescence; Berger 2006) and radio spectral luminosity (significantly outshining the next most luminous source, 2MASS J05181131-3101529 at $[L_{\nu,\rm R}] = 13.9$; McLean et al. 2012). It is also one of the brightest UCDs in X-rays, whether quantified in terms of flux, luminosity, or bolometrically normalized luminosity. Only the serendipitously discovered object 2XMM J043527.2-144301 may be more X-ray luminous; however, this object is not well-studied, and in particular has an uncertain spectrophotometric distance of 67(13) pc (Gupta et al. 2011). In quiescence, $L_{\rm H\alpha} \sim L_{\rm UVW1} \sim L_{\rm X}$. The (noncontemporaneous) quiescent luminosities between the bands fall on the scaling relations determined by Stelzer et al. (2013).

Figures 13 and 14 show the spectral energy distribution (SED) of the blended components of NLTT 33370 AB. Figure 13 shows details in the optical/infrared (OIR) bands. Included in these plots is a representative BT-Settl model photospheric spectrum (Allard et al. 2012) with $T_{\rm eff}$ = 2700 K, $\log g$ = 4.5, and solar metallicity, computed with the `CIFIST2011` version of the code, which uses the solar abundances of Caffau et al. (2011). The parameters of this model match those used by Schlieder et al. (2014) to model the individual components of the binary, except for $T_{\rm eff}$, for which we find that a lower value provides a better match on the blue end of the OIR SED. The value used here is within 1σ of the values found by Schlieder et al. (2014), which are 3200(500) and 3100(500) K for the A and B components, respectively. The normalization of this model was set by weighted least-squares optimization of the synthetic photometry against the measurements shown in Figure 13. The reduced χ^2 of this fit is 5.29; similar fits with other values of $T_{\rm eff}$, stepped in 100 K increments, yield inferior results ($\chi^2_r = 18.74$,

Table 3
Summary of Emission Characteristics

Mode	Quantity	Units	Radio	Optical	Hα	UV	X-Ray
(1)	(2)	(3)	(4)	(5)	(6)	(7)	(8)
Non-flaring	$[L]$	erg s^{-1}	25.2	29.5	27.9	27.7	27.7
	$[L/L_{bol}]$	...	−6.0	−1.7	−3.3	−3.6	−3.5
	$[F]$	erg s^{-1} cm^{-2}	4.0	8.3	6.7	6.5	6.5
	Modulation amplitude	...	0.15–0.30	0.02–0.03	0.06	≈0.08	<0.4
Flaring	L_f/L_q	...	6	<0.05	2.3	2.7	6
	$[L_f/L_{bol}]$	...	−5.3	<−3	−3.2	−3.3	−2.8
	Duty cycle	...	0.20–0.35	...	≈0.2	≈0.2	≈0.2
	Timescale	s	10^2–10^3	...	>90	10^4	10^4
	$[E]$	erg	27.4	...	>30.2	32.1	32.3

Notes. F is the surface flux assuming $R_* = 1.6\ R_J$. L_f/L_q is the ratio of flaring to quiescent luminosity. E is a characteristic flare energy release. See Section 5.1 for details.

10.25 for $T_{eff} = 2600$, 2800 K). We emphasize that this model should not be expected to precisely match the observations because the data considered here blend the emission of two distinct objects.

Figure 14 places the OIR photometry in a broader context using our radio and X-ray observations as well as archival photometry from *GALEX* (Martin et al. 2005). Magnetic phenomena dominate the photospheric contribution outside of the comparatively narrow OIR window. The radio component has a strikingly broad and flat spectrum (in terms of flux density), and our data show only suggestions of a turnover in the spectrum around ∼40 GHz (∼10^8 Å). The radio component is nonetheless energetically insignificant compared to the X-ray component, as is generally the case in comparable systems (Güdel & Benz 1993; Williams et al. 2014).

5.2. Variability

Our data show flares and/or nonflaring modulation in every band. They are consistent with findings from other detailed multiwavelength studies of cool flare stars: there is striking variation in the flaring phenomenology, both within the same band and in multi-band correlations (Osten et al. 2004, 2005). It is clear that there is no one single observational manifestation of flaring activity, and the underlying physical phenomena are plausibly as variegated as their resulting emission.

The only data in which we do *not* observe flares are the broadband optical MEarth observations. This is not surprising: white-light flares are expected to be relatively blue, while both the MEarth filter and the photospheric emission of NLTT 33370 AB are red. Using the model spectrum of Davenport et al. (2012), we find that such flares would need to reach ∼4% of L_{bol} to be detectable.

Figure 15 presents all of the light curves in compact form, with vertical scalings chosen to emphasize the nature and relative phasing of the variability in each band. The MEarth data are shown in light blue. The upper light curves show the data and full emission model, while the lower curves plot the primary and secondary sine components. The rapid, 100% LCP radio flares are shown in dark blue. Double-peaked LCP flares are seen during all 7 observed minima of the primary MEarth component. These flares may also preferentially occur around the midpoints of the rising portions of both the primary and secondary MEarth components.

Figure 15 shows the nonflaring radio data in red. The upper (lower) light curves show Stokes I (Stokes V) averaged across the two basebands. In Campaign 1, the Stokes I variations mirror those in Stokes V to a good approximation. In Campaign 2, the Stokes I variations are of about twice the amplitude, and the phasing of the light-curve minima is shifted by ∼180° relative to the primary MEarth component, which we interpret as being due to the presence of an additional emission and absorption component (Section 4.2). The Campaign 2 Stokes I variations are approximately in phase with the secondary MEarth component.

The middle panel of Figure 15 shows the EW(Hα) data in dark green. The Hα flare occurs around the time of a maximum in the MEarth light curve, although the sparse sampling makes timing analysis difficult. At the time of the Hα flare there is a noticeable dip in the Stokes I radio emission, but no 100% LCP flaring component. EW(Hα) modulates ∼180° out of phase with the optical emission.

The lower panel of Figure 15 shows the X-ray data in light green. There is no evidence for periodic variations in the *Chandra* data. A rapid X-ray flare occurs around the predicted time of a maximum in the primary MEarth light curve, although no MEarth data were obtained at that time. The X-ray flare occurs ∼1/4 of a rotation after the second-largest radio flare in the data set. The UV data are in purple; the last measurement appears to be associated with the rising phase of the slowly evolving X-ray/UV flare (Figure 3). The best sinusoidal fit to the UV data is approximately 180° out of phase with the primary MEarth component.

6. DISCUSSION

6.1. Interpreting the MEarth Periodicities

We find two similar but distinct periodicities in the MEarth light curves: a primary component at 3.7859(1) hr with amplitude ∼14 mmag and a secondary at 3.7130(2) hr with amplitude ∼7 mmag. Modeling of the individual campaigns indicates that the periods are stable to levels of $\lesssim$0.5% across the 3.4 yr time baseline of the observations. Below we discuss what we consider to be the most plausible explanations for the data: either there are multiple spots on one object with differential rotation (DR), or both components of the binary rotate with very similar periodicities.

6.1.1. Differential Rotation

The similarity of the periodicities might be taken to suggest the presence of two spots on one differentially rotating photosphere. The implied level of DR, however, is not expected to occur in stars in this mass range. The inferred absolute shear

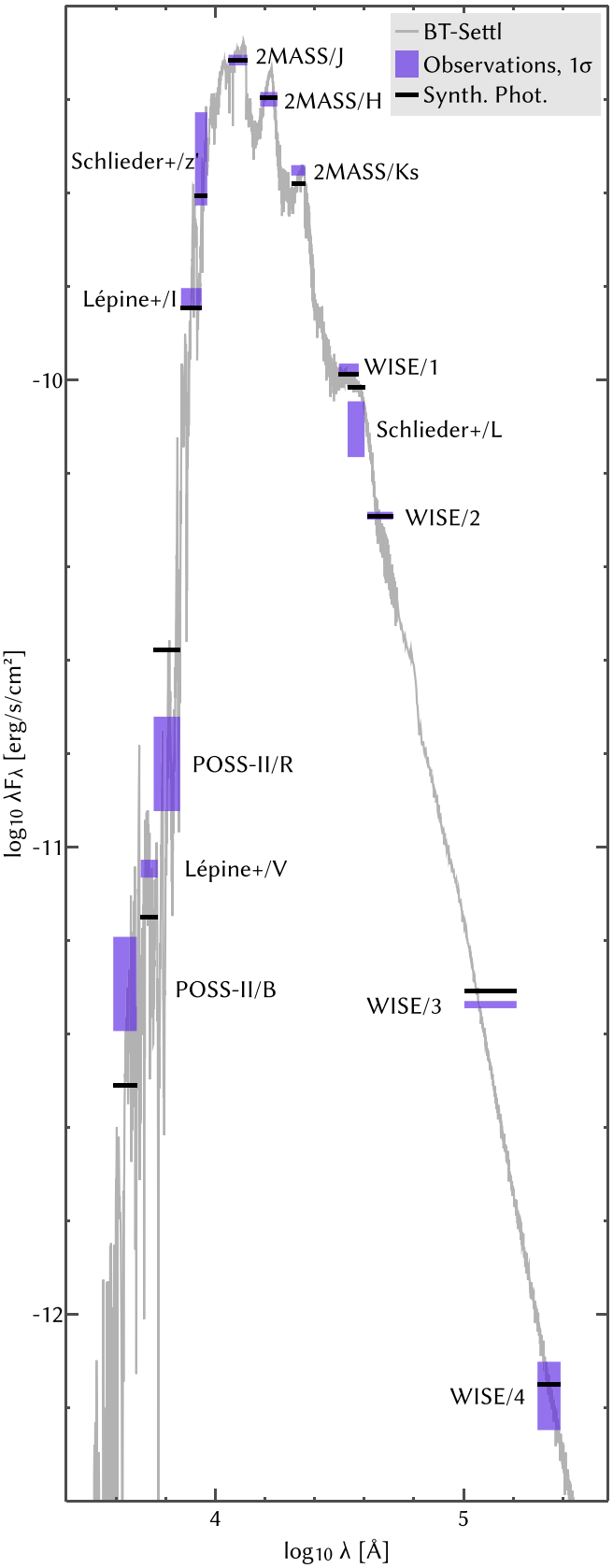

Figure 13. Nonsimultaneous, blended SED of NLTT 33370 AB in the optical/IR (OIR) bands. Violet bands show 1σ confidence regions for data from Lépine et al. (2009), Schlieder et al. (2014), 2MASS (Skrutskie et al. 2006), WISE (Wright et al. 2010), and the Second Palomar Observatory Sky Survey (POSS-II) as digitized in the USNO-B1.0 catalog (Monet et al. 2003). Black lines show synthetic photometry computed from the BT-Settl model shown (see Section 5.1 for details).

is $\Delta\Omega = 2\pi/P_1 - 2\pi/P_2 \gtrsim 0.8$ rad day^{-1} and the relative shear is $\alpha = (P_1 - P_2)/P_1 \gtrsim 0.02$, where both quantities are lower bounds because they are generally expressed in terms of pole-to-equator variation, and latitudes of the putative spots are unknown. These values are well within bounds for *partially* convective rapid rotators ($T_{\rm eff} \gtrsim 6000$ K; Reinhold et al. 2013), but not fully convective ones. In the coolest stars in the sample of Reinhold et al. (2013), $\Delta\Omega \lesssim 0.1$ rad day^{-1}. Zeeman Doppler imaging (ZDI) observations of mid-M dwarfs find very low levels of DR in moderately rapid rotators ($8 \lesssim P \lesssim 100$ hr), with $\Delta\Omega \lesssim 0.01$ rad day^{-1} (Morin et al. 2008a, 2008b; Donati et al. 2008). In V374 Peg (M4), $\alpha \sim 0.0005$ (Morin et al. 2008a). These findings are supported by some magnetohydrodynamic simulations that find that Maxwell stresses virtually arrest DR in fully convective objects (Browning 2008).

A single night of spatially resolved photometric monitoring of the binary could determine if the optical variability is confined to one object. If so, the inferred presence of DR would be extremely surprising for such a cool dwarf. We speculate that in this scenario some cool dwarfs may indeed have high DR, and that this may lead to large radio luminosities; in this case, the discovery of unusual DR in NLTT 33370 AB would be a consequence of its selection in the radio survey of McLean et al. (2011, 2012).

6.1.2. Similar Rotation Periods

Alternatively, it is possible that the two periodicities correspond to separate signals from the two components of the binary. Although the similarity of the rotation periods seems implausible, magnetic coupling to the protostellar disk might synchronize the components' rotation (Königl 1991; Edwards et al. 1993; Scholz 2013, and references therein), and subsequent spin-up due to contraction (which dominates the rotational evolution of a system this age; Reiners & Mohanty 2012; Gallet & Bouvier 2013) would only alter the period ratio by ~5% (assuming the evolutionary models of Baraffe et al. 1998). However, resolved measurements of $v \sin i$ in low-mass binaries suggest that ~50% of them have significantly different projected rotational velocities, and it is improbable that the differences are entirely due to the $\sin i$ term (Konopacky et al. 2012).

If both components of NLTT 33370 AB truly have similar masses, ages, and rotation rates, one might expect them to have similar levels of magnetic activity. However, VLBI observations indicate that the system's steady radio emission is dominated by only one of the components, with the nondetected component being $\gtrsim$5 times fainter than the detected one (McLean et al. 2011). NLTT 33370 AB may therefore be an excellent laboratory for understanding the apparent bimodality in the radio and X-ray emission levels of otherwise-similar UCDs reported by several authors (McLean et al. 2012; Stelzer et al. 2012; Williams et al. 2014; Cook et al. 2014), which may stem from a bistability in the underlying dynamo (Morin et al. 2010; Gastine et al. 2013).[6] Because NLTT 33370 AB is a visual binary and its components have such similar masses and (possibly) rotation rates, many potential confounding factors in the effort to understand the radio/X-ray bimodality could be eliminated.

[6] Another reference point is the binary BL/UV Cet (dM5.5e+dM5.5e; often referred to as UV Cet AB), in which the components have indistinguishable projected rotational velocities ($v \sin i = 31.5(30), 29.5(30)$ km s^{-1}; Jones et al. 2005) but the secondary UV Cet is far more active than the primary (e.g., Audard et al. 2003). VLBI observations detected spatially extended gyrosynchrotron emission from UV Cet but not BL Cet (Benz et al. 1998). Intriguingly, in the same observation BL Cet was seen to emit rapid polarized pulses, while UV Cet was not.

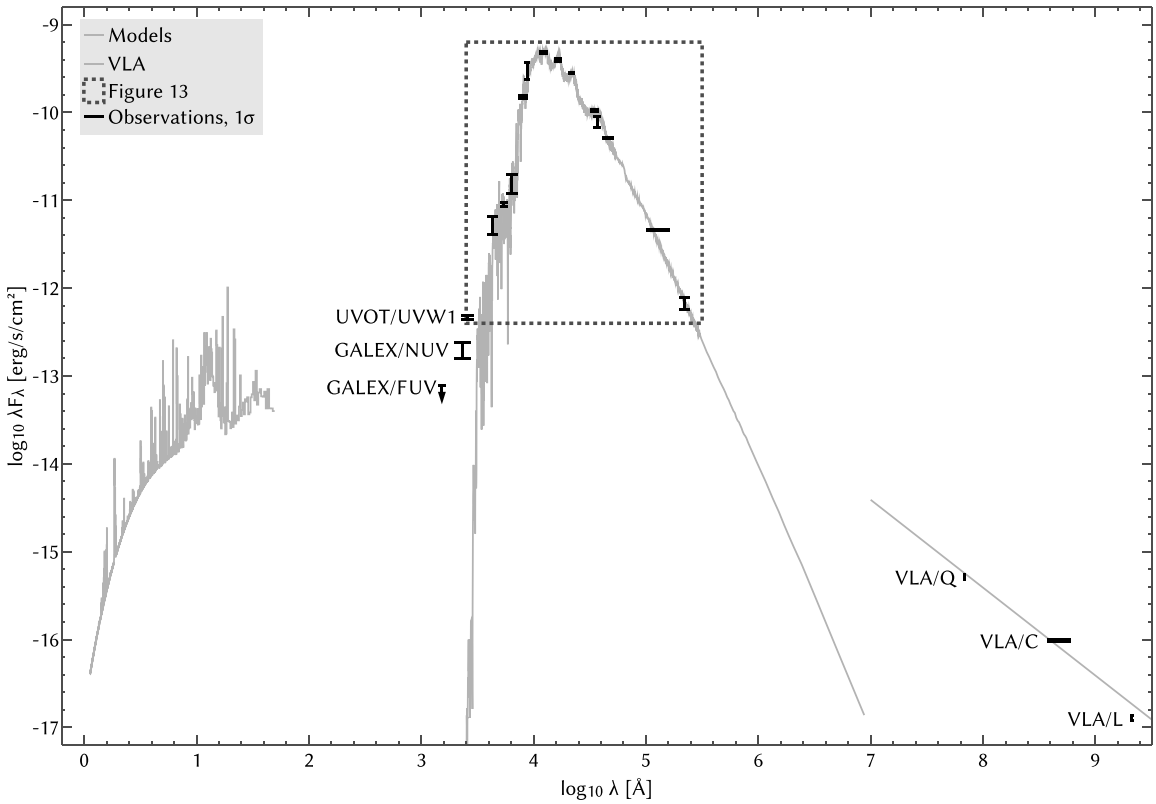

Figure 14. Ultra-wideband, nonsimultaneous, blended SED of NLTT 33370 AB. The dashed box identifies the region shown in Figure 13, in which the enclosed observational data are identified. The short-wavelength model curve shows the best-fitting two-temperature APEC source model fit as described in Section 4.3; the observed X-ray data cannot be displayed in flux density units because the incident photon energies are only known in a probabilistic sense. The middle model curve is the best-fit BT-Settl model as described in Section 5.1. The long-wavelength model curve is a constant flux density of 1.3 mJy. Also shown are measurements from *GALEX* (Martin et al. 2005), McLean et al. (2011, "VLA/L"), and this work (see Section 5.1 for details).

6.2. Nonflaring Variability

The data presented in this work are consistent with the model proposed by McLean et al. (2011), in which the stellar magnetic field is dominated by a dipole that is misaligned with the rotation axis. While McLean et al. (2011) were unable to phase-align their optical and radio data, the Campaign 2 results suggesting anti-phased radio and optical maxima would be consistent with the regions of maximal field strength hosting cool spots. Extrapolation of our MEarth model to the VLA data of McLean et al. (2011) using the Campaign 0 phasing suggests that a phase difference of 100° between the two modulations, although the ∼330-day gap between the observations is comparable to the timescale on which the modulation phase drifts in our data.

The model of a magnetized cool spot is supported by the fact that the Hα modulation, the possible UV modulation, and the Campaign 2 Stokes *I* radio emission all peak around the time of optical minimum. Furthermore, we observed Stokes *V* radio flares during all 7 optical minima. However, the rapid X-ray and Hα flares occur around optical *maximum*, the Stokes *V* flares occur at all phases, and the Campaign 1 Stokes *I* radio emission modulates approximately in phase with the optical data. The double-humped shape of the Campaign 1 emission may indeed indicate the presence of two separate emitters. While magnetic phenomena appear to be enhanced during optical minimum, they clearly occur at all phases.

A model developed for higher-mass magnetic chemically peculiar (MCP) stars ascribes radio modulation to the presence of a torus of cold, absorbing plasma around the magnetic equator (Trigilio et al. 2004, 2011). Such tori are also found encircling Jupiter and Saturn (e.g., Kivelson 2005, and references therein) and thus may plausibly occur in NLTT 33370 AB as well. Simulated radio light curves, spectra, and radio/X-ray luminosity ratios are broadly in line with the observations of NLTT 33370 AB (Trigilio et al. 2004), and periodic auroral bursts are predicted that could be consistent with the LCP flares at optical minima (Trigilio et al. 2011).

We argue in Section 4.2 that the Campaign 2 emission includes an additional component that may be due to optically thick gyrosynchrotron flaring, explaining the apparent phase shift of the radio Stokes *I* relative to the optical maxima. However, the decrease of Stokes *I* in Campaign 2 relative to the expected Campaign 1 emission (Figure 9) requires the presence of an absorber. The additional emission component may thus be associated with the creation or expansion of an absorbing plasma torus as suggested by the MCP model. Because free–free optical depth scales approximately quadratically with wavelength (Dulk 1985), the torus would need to be opaque across the VLA band to maintain the observed flat spectrum. Assuming $n_e = 10^9$ cm^{-3} and $T = 10^4$ K as in Trigilio et al. (2011), the required path length would be ∼0.05 R_*. The component associated with the Stokes *V* modulation may be confined to the magnetic poles, where the expanded torus would not alter the observed signal.

Models with large polar spots may seem difficult to reconcile with the presence of two periodic signals in the MEarth data. However, we note that magnetic phenomena in the two hemispheres of Saturn are associated with rotation periods that differ at the 1% level (Gurnett et al. 2009). We speculate that one of the components of NLTT 33370 AB may host two large polar spots that similarly rotate at slightly different rates.

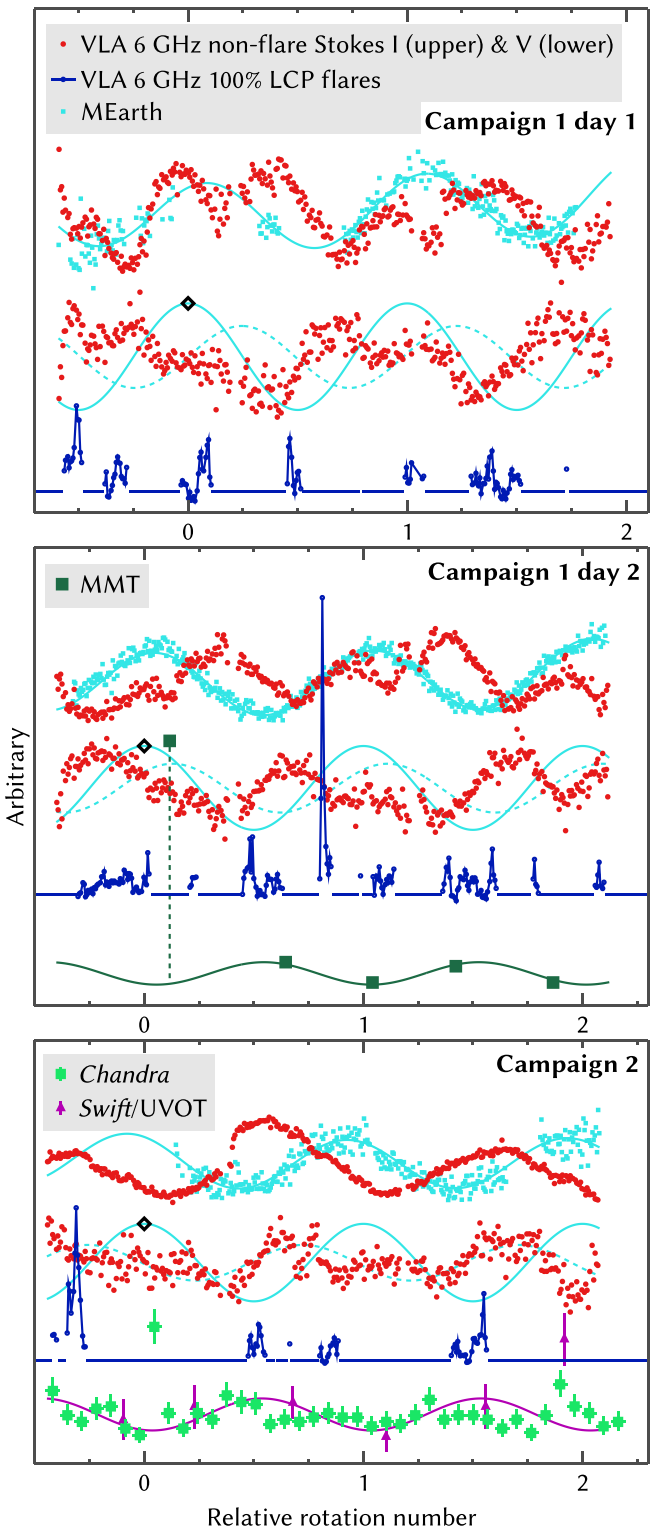

Figure 15. Relative phasing of various emission components in the three nights of intensive observations. Vertical scalings are chosen to emphasize the variation within each band. The horizontal scale for each panel counts rotations at a period of 3.7859 hr relative to the black diamonds. Within each panel, the upper red and blue light curves trace nonflaring VLA Stokes *I* and MEarth emission, respectively, while the lower curves trace nonflaring VLA Stokes *V* and the MEarth data decomposed into two components (see Section 4.1). Dark blue shows 100% LCP VLA flares. Dark green in the middle panel shows EW(Hα) (MMT). In the lower panel, green and purple indicate X-ray (*Chandra*) and UV (*Swift*) light curves, respectively. See Section 4 for details on the modeling.

One caveat is that in Saturn, this effect may be driven by the Sun (Gurnett et al. 2009); NLTT 33370 AB does not have a similar driver.

6.3. Flaring Conditions

Although the nonflaring modulation suggests the presence of large-scale magnetic fields, the rapid flares we observe imply the presence of significant magnetic energy in small-scale fields as well, as is expected for low-mass stars in general on both observational (Reiners & Basri 2009) and theoretical grounds (Lang et al. 2014). The frequent ($\sim$30% duty cycle) LCP radio flares suggest the nearly continuous occurrence of magnetic reconnection, especially since such coherent emission is expected to be strongly beamed. Reconnection dominated by large-scale ($\sim R_*$) magnetic fields, on the other hand, would lead to less frequent, larger flares, as observed in some UCDs in X-rays (Stelzer et al. 2006b; Robrade et al. 2010); the slow-evolving X-ray/UV flare observed by *Swift* may be an instance of one of these. Hydrodynamic modeling of flaring loops suggests a length scale of 10^9cm $\sim 0.1\,R_*$ from the $\sim$150 s decay timescale of the rapid *Chandra* flare (Serio et al. 1991). Frequent small-scale reconnection events, as suggested by the radio LCP and X-ray flares, may be related to radio emission above that predicted by the Güdel-Benz relation (Güdel & Benz 1993) both specifically in NLTT 33370 AB and more generally (Williams et al. 2014).

Applying the Güdel–Benz relation to the rapid X-ray flare, the expected radio luminosity is $[L_{\nu,\mathrm{R}}] \sim 13$, equivalent to a flux density of 0.03 mJy. Such an enhancement would not be discernible in the radio light curves. Assuming that Hα luminosity represents $\sim$10% of the white-light component of a flare (Neidig 1989) and that flare soft X-ray luminosity is $\sim$20% of that of the white light (Woods et al. 2004), the flaring Hα measurement would correspond to a nearly identical value of $[L_{\mathrm{X}}] = 28.5$, and have a similarly insignificant radio component. Combined with the energetic insignificance of the coherent radio emission (Table 3), the overall lack of correlation among rapid flare events at multiple bands is striking, but potentially not surprising (e.g., Osten et al. 2004, 2005).

6.4. Effect of Activity on Fundamental Measurements

The high levels of activity in NLTT 33370 AB have significant implications for its status as benchmark system for young, low-mass objects. The results of Stassun et al. (2012) suggest that mass estimates will not be strongly affected because L_{bol} is approximately conserved; however, this particular system will yield dynamical mass measurements regardless. On the other hand, their relations predict that magnetism may alter T_{eff} by $\sim -10\%$ and R_* by $\sim$+20%. (Our estimates are $\sim$2 times larger than those of Schlieder et al. (2014), likely due to the use of a different χ factor, since we use their $[L_{\mathrm{bol}}]$ and equivalent EW(Hα) values.) The detection of only a single component in VLBI (McLean et al. 2011) suggests that these effects may be concentrated in only one component of the binary. However, Stassun et al. (2012) rely on Hα rather than radio emission as a metric of magnetic activity, and it remains to be conclusively determined what the most physically relevant tracer truly is.

7. SUMMARY AND CONCLUSIONS

We have presented a detailed simultaneous study of the magnetic activity of the young UCD binary NLTT 33370 AB

from two observational campaigns in the radio, optical, Hα, UV, and X-ray bands. Some of the key phenomena are:

1. Extreme magnetic activity, with the highest radio luminosity of any known UCD, one of the highest X-ray luminosities, and a large Hα luminosity as well (Table 3).
2. Periodic modulation of emission in at least the radio and optical bands, and plausible UV and Hα modulation. The long-term MEarth data set reveals two distinct periodicities of 3.7859(1) and 3.7130(2) hr, with $\sim$50% evolution in the modulation amplitude and phase from year to year.
3. Significant evolution in the Stokes I radio modulation between the two campaigns, with the amplitude increasing by a factor of 2 and the phase shifting by $\sim$180°. However, Stokes V is stable and phases consistently with the primary MEarth periodicity in both campaigns.
4. A very bright Stokes V flare with a spectral cutoff suggesting a magnetic field strength of 2.1 kG in the ECMI interpretation.
5. A typical X-ray spectrum adequately fit by two temperature components of 0.27(2) and 1.20(6) keV. However, the hardness gradually increases before a large X-ray/UV flare lasting $\sim$0.1 day.
6. A general lack of correlation between flares in any band. The exceptions are the slow X-ray/UV flare observed by *Swift*, and the consistent detection of Stokes V flares at optical minima.

Our analysis leads us to conclude that:

1. The explanation for the two MEarth periodicities is unclear. Although they differ by only $\sim$2%, even this level of differential rotation is not expected in stars this cool. If NLTT 33370 AB indeed shows unusual differential rotation, it may possibly be a consequence of its selection as an unusually magnetically active system.
2. The periodic modulation of the nonflaring emission of NLTT 33370 AB may be understood in a model with a large-scale magnetic field misaligned with the rotation axis. The change in the relative phasing of the radio Stokes I and optical modulation between Campaigns 1 and 2 is the most difficult to explain in such a context. The stability of the radio Stokes V signal, however, suggests that the Campaign 2 radio emission is the sum of that seen in Campaign 1 and an additional component that is furthermore associated with an absorbing equatorial torus of cold plasma (Trigilio et al. 2004, 2011).
3. The presence of frequent, rapid flares at all rotational phases implies the additional presence of significant magnetic energy in small scales that is being dissipated in reconnection events nearly continuously. This may be related to the excessive radio luminosity of NLTT 33370 AB relative to the Güdel-Benz relation (Williams et al. 2014).
4. The high levels of magnetic activity in this system may alter $T_{\rm eff}$ by $\sim -10\%$ and R_* by $\sim +20\%$.

Significant progress can be made with currently available resources. Not only will spatially resolved astrometric monitoring improve constraints on the fundamental parameters of the binary components, it will allow much tighter constraints on the radio emission of the more radio-faint component by providing knowledge of its position in existing VLBI data sets. Such monitoring is in progress, as are continued VLBI observations. Spatially resolved spectroscopy of this system is achievable with state-of-the-art facilities (e.g., Konopacky et al. 2012) and would yield both resolved radial velocity measurements, diagnosing the inclination of the binary orbit, and resolved $v \sin i$ measurements, providing key insight into the rotation rates of the two components. Spatially resolved photometric monitoring would be resource-intensive but could resolve the $\sin i$ ambiguity in spectroscopic rotation measurements. With a separation of $\sim$0.″1, NLTT 33370 AB is unfortunately not spatially resolvable by *Chandra* or any planned X-ray observatories—unless its orbit turns out to be highly eccentric.

New spatially resolved observations of NLTT 33370 AB will advance the understanding of habitable exoplanets around low-mass stars because of this system's twofold importance: it is a benchmark for measurements of both fundamental stellar properties *and* magnetic activity at the bottom of main sequence. The former affect the derived properties of exoplanets themselves, and the latter may strip the atmospheres of close-in planets or otherwise render them inhospitable to life.

We thank Jan Forbrich for sharing preliminary VLBI results and helpful suggestions. P.K.G.W. and E.B. acknowledge support for this work from the National Science Foundation through Grant AST-1008361. Z.K.B.-T. acknowledges support from the Torres Fellowship for Exoplanetary Research. The VLA is operated by the National Radio Astronomy Observatory, a facility of the National Science Foundation operated under cooperative agreement by Associated Universities, Inc. This research has made use of the SIMBAD database, operated at CDS, Strasbourg, France, and NASA's Astrophysics Data System. This research has made use of the XRT Data Analysis Software (XRTDAS) developed under the responsibility of the ASI Science Data Center (ASDC), Italy.

This paper makes use of data from the MEarth Project, which is a collaboration between Harvard University and the Smithsonian Astrophysical Observatory. The MEarth Project acknowledges funding from the David and Lucile Packard Fellowship for Science and Engineering and the National Science Foundation under grants AST-0807690, AST-1109468, and AST-1004488 (Alan T. Waterman Award), and a grant from the John Templeton Foundation.

This publication makes use of data products from the Wide-field Infrared Survey Explorer, which is a joint project of the University of California, Los Angeles, and the Jet Propulsion Laboratory/California Institute of Technology, funded by the National Aeronautics and Space Administration.

This publication makes use of data products from the Two Micron All Sky Survey, which is a joint project of the University of Massachusetts and the Infrared Processing and Analysis Center/California Institute of Technology, funded by the National Aeronautics and Space Administration and the National Science Foundation.

Facilities: CXO, VLA, MMT, *Swift*

REFERENCES

Alef, W., Benz, A. O., & Güdel, M. 1997, A&A, 317, 707
Allard, F., Homeier, D., & Freytag, B. 2012, RSPTA, 370, 2765
Audard, M., Güdel, M., & Skinner, S. L. 2003, ApJ, 589, 983
Audard, M., Osten, R. A., Brown, A., et al. 2007, A&A, 471, L63
Baraffe, I., Chabrier, G., Allard, F., & Hauschildt, P. H. 1998, A&A, 337, 403
Baraffe, I., Chabrier, G., Allard, F., & Hauschildt, P. H. 2002, A&A, 382, 563
Barman, T. S., Macintosh, B., Konopacky, Q. M., & Marois, C. 2011, ApJ, 733, 65
Becker, R. H., White, R. L., & Helfand, D. J. 1995, ApJ, 450, 559
Benz, A. O., Conway, J., & Güdel, M. 1998, A&A, 331, 596
Benz, A. O., & Güdel, M. 1994, A&A, 285, 621

Berger, E. 2002, ApJ, 572, 503
Berger, E. 2006, ApJ, 648, 629
Berger, E., Ball, S., Becker, K. M., et al. 2001, Natur, 410, 338
Berger, E., Basri, G., Fleming, T. A., et al. 2010, ApJ, 709, 332
Berger, E., Basri, G., Gizis, J. E., et al. 2008a, ApJ, 676, 1307
Berger, E., Gizis, J. E., Giampapa, M. S., et al. 2008b, ApJ, 673, 1080
Berger, E., Rutledge, R. E., Phan-Bao, N., et al. 2009, ApJ, 695, 310
Berta, Z. K., Irwin, J., Charbonneau, D., Burke, C. J., & Falco, E. E. 2012, AJ, 144, 145
Blanton, M. R., & Roweis, S. 2007, AJ, 133, 734
Bonfils, X., Delfosse, X., Udry, S., et al. 2013, A&A, 549, A109
Bouy, H., Martín, E. L., Brandner, W., et al. 2008, A&A, 481, 757
Bowler, B. P., Liu, M. C., Dupuy, T. J., & Cushing, M. C. 2010, ApJ, 723, 850
Breeveld, A. A., Landsman, W., Holland, S. T., et al. 2011, in AIP Conf. Proc. 1358, Gamma Ray Bursts 2010, ed. J. E. McEnery, J. L. Racusin, & N. Gehrels (Melville, NY: AIP), 373
Brown, B. P., Browning, M. K., Brun, A. S., Miesch, M. S., & Toomre, J. 2010a, ApJ, 711, 424
Brown, P. J., Roming, P. W. A., Milne, P., et al. 2010b, ApJ, 721, 1608
Browning, M. K. 2008, ApJ, 676, 1262
Burgasser, A. J., Melis, C., Zauderer, B. A., & Berger, E. 2013, ApJL, 762, L3
Burgasser, A. J., & Putman, M. E. 2005, ApJ, 626, 486
Caffau, E., Ludwig, H.-G., Steffen, M., Freytag, B., & Bonifacio, P. 2011, SoPh, 268, 255
Cash, W. 1979, ApJ, 228, 939
Chabrier, G., & Baraffe, I. 2000, ARA&A, 38, 337
Chabrier, G., & Küker, M. 2006, A&A, 446, 1027
Chauvin, G., Lagrange, A.-M., Zuckerman, B., et al. 2005, A&A, 438, L29
Cohen, O., Drake, J. J., Glocer, A., et al. 2014, ApJ, 790, 57
Cohen, O., Kashyap, V. L., Drake, J. J., et al. 2011, ApJ, 733, 67
Cook, B. A., Williams, P. K. G., & Berger, E. 2014, ApJ, 785, 10
Davenport, J. R. A., Becker, A. C., Kowalski, A. F., et al. 2012, ApJ, 748, 58
Delorme, P., Gagné, J., Malo, L., et al. 2012, A&A, 548, A26
Dobler, W., Stix, M., & Brandenburg, A. 2006, ApJ, 638, 336
Donati, J. F., Morin, J., Petit, P., et al. 2008, MNRAS, 390, 545
Dulk, G. A. 1985, ARA&A, 23, 169
Dupuy, T. J., & Kraus, A. L. 2013, Sci, 341, 1492
Dupuy, T. J., Liu, M. C., Bowler, B. P., et al. 2010, ApJ, 721, 1725
Dupuy, T. J., Liu, M. C., & Ireland, M. J. 2009, ApJ, 629, 729
Dupuy, T. J., Liu, M. C., & Ireland, M. J. 2014, ApJ, 790, 133
Durney, B. R., de Young, D. S., & Roxburgh, I. W. 1993, SoPh, 145, 207
Eastman, J., Siverd, R., & Gaudi, B. S. 2010, PASP, 122, 935
Edwards, S., Strom, S. E., Hartigan, P., et al. 1993, AJ, 106, 372
Frasca, A., Freire Ferrero, R., Marilli, E., & Catalano, S. 2000, A&A, 364, 179
Freeman, P., Doe, S., & Siemiginowska, A. 2001, Proc. SPIE, 4477, 76
Fruscione, A., McDowell, J. C., Allen, G. E., et al. 2006, Proc. SPIE, 6270, 62701V
Gallet, F., & Bouvier, J. 2013, A&A, 556, 36
Gastine, T., Morin, J., Duarte, L., et al. 2013, A&A, 549, L5
Gizis, J. E., Monet, D. G., Reid, I. N., et al. 2000, AJ, 120, 1085
Güdel, M., & Benz, A. O. 1993, ApJL, 405, L63
Gupta, A., Galeazzi, M., & Williams, B. 2011, ApJ, 731, 63
Gurnett, D. A., Lecacheux, A., Kurth, W. S., et al. 2009, GeoRL, 36, L16102
Hallinan, G., Antonova, A., Doyle, J. G., et al. 2006, ApJ, 653, 690
Hallinan, G., Antonova, A., Doyle, J. G., et al. 2008, ApJ, 684, 644
Hallinan, G., Bourke, S., Lane, C., et al. 2007, ApJL, 663, L25
Hilton, E. J., West, A. A., Hawley, S. L., & Kowalski, A. F. 2010, AJ, 140, 1402
Hong, J., Schlegel, E. M., & Grindlay, J. E. 2004, ApJ, 614, 508
Irwin, J., & Bouvier, J. 2008, in IAU Symp. 258, The Ages of Stars, ed. E. E. Mamajek, D. R. Soderblom, & R. F. G. Wyse (Cambridge: Cambridge Univ. Press), 363
Irwin, J., Irwin, M., Aigrain, S., et al. 2007, MNRAS, 375, 1449
Johns-Krull, C. M., Valenti, J. A., & Linsky, J. L. 2000, ApJ, 539, 815
Jones, H. R. A., Pavlenko, Y., Viti, S., et al. 2005, MNRAS, 358, 105
Khodachenko, M. L., Ribas, I., Lammer, H., et al. 2007, AsBio, 7, 167
Kirkpatrick, J. D., Gelino, C. R., Cushing, M. C., et al. 2012, ApJ, 753, 156
Kirkpatrick, J. D., Reid, I. N., Liebert, J., et al. 1999, ApJ, 519, 802
Kivelson, M. G. 2005, AdSpR, 36, 2077
Königl, A. 1991, ApJL, 370, 39
Konopacky, Q. M., Ghez, A. M., Barman, T. S., et al. 2010, ApJ, 711, 1087
Konopacky, Q. M., Ghez, A. M., Fabrycky, D. C., et al. 2012, ApJ, 750, 79
Kopparapu, R. K. 2013, ApJL, 767, L8
Kruger, A. T., Loredo, T. J., & Wasserman, I. 2002, ApJ, 576, 932
Kuiper, N. H. 1960, Proc. Koninklijke Nederlandse Akademie van Wetenschappen: Series A, 63, 38
Lammer, H. 2007, AsBio, 7, 27
Lang, P., Jardine, M., Morin, J., et al. 2014, MNRAS, 439, 2122
Lanza, A. F. 2013, A&A, 557, A31
Law, N. M., Hodgkin, S. T., & Mackay, C. D. 2006, MNRAS, 368, 1917
Lecavelier des Etangs, A. 2007, A&A, 461, 1185
Lee, K.-G., Berger, E., & Knapp, G. R. 2010, ApJ, 708, 1482
Lépine, S., & Shara, M. M. 2005, AJ, 129, 1483
Lépine, S., Thorstensen, J. R., Shara, M. M., & Rich, R. M. 2009, AJ, 137, 4109
Linsky, J. L., Fontenla, J., & France, K. 2014, ApJ, 780, 61
Liu, M. C., Magnier, E. A., Deacon, N. R., et al. 2013, ApJL, 777, L20
Llama, J., Vidotto, A. A., Jardine, M., et al. 2013, MNRAS, 436, 2179
Lodders, K. 2003, ApJ, 591, 1220
López-Morales, M. 2007, ApJ, 660, 732
Luhman, K. L. 2012, ARA&A, 50, 65
Luhman, K. L. 2013, ApJL, 767, L1
Luhman, K. L. 2014, ApJL, 786, L18
Luyten, W. J. 1979, New Luyten Catalogue of Stars with Proper Motions Larger than Two Tenths of an Arcsecond (Minneapolis, MN: Univ. Minnesota Press)
MacDonald, J., & Mullan, D. J. 2013, ApJ, 765, 126
Maritz, J. S., & Jarrett, R. G. 1978, JASA, 73, 194
Marley, M. S., Ackerman, A. S., Cuzzi, J. N., & Kitzmann, D. 2013, in Comparitive Climatology of Terrestrial Planets, ed. S. J. Mackwell, A. A. Simon-Miller, J. W. Harder, & M. A. Bullock (Tucson, AZ: Univ. Arizona Press), 367
Martin, D. C., Fanson, J., Schiminovich, D., et al. 2005, ApJL, 619, 1
Martín, E. L., Delfosse, X., Basri, G., et al. 1999, AJ, 118, 2466
McIvor, T., Jardine, M., & Holzwarth, V. 2006, MNRAS Lett., 367, L1
McLean, M., Berger, E., Irwin, J., Forbrich, J., & Reiners, A. 2011, ApJ, 741, 27
McLean, M., Berger, E., & Reiners, A. 2012, ApJ, 746, 23
McMullin, J. P., Waters, B., Schiebel, D., Young, W., & Golap, K. 2007, in ASP Conf. Ser. 376, Astronomical Data Analysis Software and Systems XVI, ed. R. A. Shaw, F. Hill, & D. J. Bell (San Francisco, CA: ASP), 127
Mitra-Kraev, U., Harra, L. K., Güdel, M., et al. 2005, A&A, 431, 679
Mohanty, S., & Basri, G. 2003, ApJ, 583, 451
Mohanty, S., Basri, G., Shu, F., Allard, F., & Chabrier, G. 2002, ApJ, 571, 469
Monet, D. G., Levine, S. E., Canzian, B., et al. 2003, AJ, 125, 984
Moré, J. J. 1978, Lecture Notes Math., 630, 105
Morin, J., Donati, J.-F., Forveille, T., et al. 2008a, MNRAS, 384, 77
Morin, J., Donati, J.-F., Petit, P., et al. 2008b, MNRAS, 390, 567
Morin, J., Donati, J.-F., Petit, P., et al. 2010, MNRAS, 407, 2269
Neidig, D. F. 1989, SoPh, 121, 261
Nelder, J. A., & Mead, R. 1965, Comp. J., 7, 308
Ness, J.-U., Güdel, M., Schmitt, J. H. M. M., Audard, M., & Telleschi, A. 2004, A&A, 427, 667
Ness, J.-U., Schmitt, J. H. M. M., Burwitz, V., et al. 2002, A&A, 394, 911
Nutzman, P., & Charbonneau, D. 2008, PASP, 120, 317
Offringa, A. R., de Bruyn, A. G., Biehl, M., et al. 2010, MNRAS, 405, 155
Offringa, A. R., van de Gronde, J. J., & Roerdink, J. B. T. M. 2012, A&A, 539, A95
Ossendrijver, M. 2003, A&ARv, 11, 287
Osten, R. A., Brown, A., Ayres, T. R., et al. 2004, ApJS, 153, 317
Osten, R. A., Brown, A., Wood, B. E., & Brady, P. 2002, ApJS, 138, 99
Osten, R. A., Hawley, S. L., Allred, J. C., Johns-Krull, C. M., & Roark, C. 2005, ApJ, 621, 398
Patience, J., King, R. R., de Rosa, R. J., & Marois, C. 2010, A&A, 517, A76
Perley, R. A., & Butler, B. J. 2013, ApJS, 204, 19
Pizzolato, N., Maggio, A., Micela, G., Sciortino, S., & Ventura, P. 2003, A&A, 397, 147
Poppenhaeger, K., Schmitt, J. H. M. M., & Wolk, S. J. 2013, ApJ, 773, 62
Reid, I. N., & Gizis, J. E. 1997, AJ, 113, 2246
Reiners, A., & Basri, G. 2006, ApJ, 644, 497
Reiners, A., & Basri, G. 2007, ApJ, 656, 1121
Reiners, A., & Basri, G. 2008, ApJ, 684, 1390
Reiners, A., & Basri, G. 2009, A&A, 496, 787
Reiners, A., & Basri, G. 2010, ApJ, 710, 924
Reiners, A., & Mohanty, S. 2012, ApJ, 746, 43
Reinhold, T., Reiners, A., & Basri, G. 2013, A&A, 560, A4
Ribas, I., Morales, J. C., Jordi, C., et al. 2008, MmSAI, 79, 562
Robrade, J., Poppenhaeger, K., & Schmitt, J. H. M. M. 2010, A&A, 513, A12
Robrade, J., & Schmitt, J. H. M. M. 2005, A&A, 435, 1073
Route, M., & Wolszczan, A. 2012, ApJL, 747, L22
Sault, R. J., & Wieringa, M. H. 1994, A&AS, 108, 585
Scalo, J., Kaltenegger, L., Segura, A., et al. 2007, AsBio, 7, 85
Scargle, J. D. 1998, ApJ, 504, 405
Scargle, J. D., Norris, J. P., Jackson, B., & Chiang, J. 2013, ApJ, 764, 167
Schlieder, J., Bonnefoy, M., Herbst, T. M., et al. 2014, ApJ, 783, 27
Schlieder, J. E., Lépine, S., & Simon, M. 2012, AJ, 143, 80
Schmitt, J. H. M. M., & Liefke, C. 2002, A&A, 382, L9

Scholz, A. 2013, MmSAI, 84, 890
Segura, A., Kasting, J. F., Meadows, V., et al. 2005, AsBio, 5, 706
Serio, S., Reale, F., Jakimiec, J., Sylwester, B., & Sylwester, J. 1991, A&A, 241, 197
Shkolnik, E. L., & Barman, T. S. 2014, ApJ, in press
Skrutskie, M. F., Cutri, R. M., Stiening, R., et al. 2006, AJ, 131, 1163
Smith, R. K., Brickhouse, N. S., Liedahl, D. A., & Raymond, J. C. 2001, ApJL, 556, L91
Stassun, K. G., Kratter, K. M., Scholz, A., & Dupuy, T. J. 2012, ApJ, 756, 47
Stellingwerf, R. F. 1978, ApJ, 224, 953
Stelzer, B., Alcalá, J., Biazzo, K., et al. 2012, A&A, 537, A94
Stelzer, B., Marino, A., Micela, G., López-Santiago, J., & Liefke, C. 2013, MNRAS, 431, 2063
Stelzer, B., Micela, G., Flaccomio, E., Neuhäuser, R., & Jayawardhana, R. 2006a, A&A, 448, 293
Stelzer, B., Schmitt, J. H. M. M., Micela, G., & Liefke, C. 2006b, A&A, 460, L35
Tarter, J., Backus, P., Mancinelli, R., et al. 2007, AsBio, 7, 30
Tian, F. 2009, ApJ, 703, 905
Treumann, R. 2006, A&ARv, 13, 229
Trigilio, C., Leto, P., Umana, G., Buemi, C. S., & Leone, F. 2011, ApJL, 739, L10
Trigilio, C., Leto, P., Umana, G., Leone, F., & Buemi, C. S. 2004, A&A, 418, 593
Vilhu, O. 1984, A&A, 133, 117
Walkowicz, L. M., Hawley, S. L., & West, A. A. 2004, PASP, 116, 1105
West, A. A., & Hawley, S. L. 2008, PASP, 120, 1161
West, A. A., Hawley, S. L., Walkowicz, L. M., et al. 2004, AJ, 128, 426
West, A. A., Morgan, D. P., Bochanski, J. J., et al. 2011, AJ, 141, 97
Williams, P. K. G., Berger, E., & Zauderer, B. A. 2013, ApJL, 767, L30
Williams, P. K. G., Cook, B. A., & Berger, E. 2014, ApJ, 785, 9
Woods, T. N., Eparvier, F. G., Fontenla, J., et al. 2004, GeoRL, 31, L10802
Wright, E. L., Eisenhardt, P. R. M., Mainzer, A. K., et al. 2010, AJ, 140, 1868
Wu, C. S., & Lee, L. C. 1979, ApJ, 230, 621